THE ASTROPHYSICAL JOURNAL, 403:216–238, 1993 January 20

ISOTOPIC *r*-PROCESS ABUNDANCES AND NUCLEAR STRUCTURE FAR FROM STABILITY: IMPLICATIONS FOR THE *r*-PROCESS MECHANISM

KARL-LUDWIG KRATZ
Institut für Kernchemie, Universität Mainz, Fritz-Straßmann-Weg 2, D-W-6500 Mainz, Germany

JEAN-PHILIPPE BITOUZET[1] AND FRIEDRICH-KARL THIELEMANN
Harvard-Smithsonian Center for Astrophysics, 60 Garden Street, Cambridge, MA 02138

AND

PETER MÖLLER AND BERND PFEIFFER
Institut für Kernchemie, Universität Mainz, Fritz-Straßmann-Weg 2, D-W-6500, Mainz, Germany
Received 1991 August 13; accepted 1992 July 14

ABSTRACT

Attempts to explain the source of *r*-process elements in nature by particular astrophysical sites face the entwined uncertainties, stemming from the extrapolation of nuclear properties far from stability, inconsistent sources of different properties (e.g., nuclear masses and half-lives), and the (poor) understanding of astrophysical conditions, which are hard to disentangle. We utilize the full isotopic *r*-process abundances in nature [especially in all of the three peaks ($A \simeq 80$, 130, 195)] and a unified model for all nuclear properties involved (aided by recent experimental knowledge in the *r*-process path), to deduce uniquely the conditions necessary to produce such an abundance pattern. Recent analysis of a few isotopic ratios in the $A \approx 80$ and $A \approx 130$ *r*-process peaks led to the conclusion that the *r*-process abundances originate from a high-density and high-temperature environment, which supports an equilibrium between neutron captures and photodisintegrations. This excludes events where neutrons are released from (α, n) reactions in explosive He burning. The present study investigates also the nature of the steady-flow equilibrium of beta decays between isotopic chains. We find strong evidence that a steady flow was not global but only local in between neighboring peaks, which requires time scales not much longer than 1 s. The abundances have to be explained by a superposition of *r*-process components with varying neutron number densities $n_n > 10^{20}$ cm^{-3} and temperatures $T > 10^9$ K, where each of the components proceeds up to one of the peaks. The remaining odd-even effects in observed abundances indicate that neutron densities dropped during freeze-out by orders of magnitude on time scales close to 0.04 s. A set of n_n-T conditions is presented as a test for any astrophysical *r*-process site. We also show how remaining deficiencies in the produced abundance pattern can be used to extract nuclear properties far from stability.

Subject headings: nuclear reactions, nucleosynthesis, abundances — supernovae: general

1. INTRODUCTION

Since the papers of Burbidge et al. (1957) and Cameron (1957), the rapid neutron-capture process has been related to environments with a high neutron density, where neutron captures are faster than beta decays, even for neutron-rich unstable nuclei up to 15–30 units from stability. Magic neutron numbers are then encountered for smaller mass numbers A than in the valley of stability, which shifts the *r*-process abundance peaks in comparison with the *s*-process peaks. But, besides this basic understanding, the history of *r*-process research has been quite diverse in suggested scenarios (for recent reviews see Mathews & Cowan 1990; Cowan, Thielemann, & Truran 1991a and references therein):

1. Several investigators (Seeger, Fowler, & Clayton 1965; Cameron, Delano, & Truran 1970; Kodama & Takahashi 1975; Hillebrandt, Takahashi, & Kodama 1976; Hillebrandt 1978; Goriely & Arnould 1992) noticed that the overall shape of *r*-process abundances and the position of the peaks could be reproduced by a superposition of neutron densities. The suggested astrophysical sites were type II supernovae, but until today a complete understanding of the supernova mechanism is still pending. The main concern with this scenario was that, when also requiring the given range in neutron densities, the mass of *r*-process matter seemed to be larger by a factor of 1000 than the typical 10^{-6} to 10^{-7} $M_\odot$ per supernova, allowed to reproduce the total amount of *r*-process elements in the Galaxy (Hillebrandt 1978),

2. Alternatives were explosive He-burning environments, where the *r*-process had only to act on previously *s*-processed material and one neutron density was sufficient to transfer matter from each *s*-process peak into the next higher *r*-process peak (e.g., Truran, Cowan, & Cameron 1978; Thielemann, Arnould, & Hillebrandt 1979).

3. Cameron et al. (1983a) performed steady-flow calculations, independent of a particular site. The results did not give perfect agreement with the solar abundance pattern, but reproduced the peaks with decreasing abundances for increasing A. More recently, first experimental information in the $A \simeq 80$ and $A \simeq 130$ regions, together with improved accuracy in solar *r*-process abundances, made it possible even to analyze isotopic abundance patterns. Kratz et al. (1988b) concluded that, indeed, an $(n, \gamma) \rightleftharpoons (\gamma, n)$ equilibrium (waiting-point

[1] Postal address: Ecole Polytechnique, 1ère Compagnie, F-91128 Palaiseau Cedex, France.

approximation) and a steady flow were required to reproduce specific features in the $A \simeq 80$ and $A \simeq 130$ peaks.

The aim of the present investigation is to analyze whether all of the previously mentioned scenarios are still consistent with the present knowledge of *r*-process abundances *and* the available knowledge of nuclear properties far from stability, or if more stringent constraints can be set. We will discuss the basics of the *r*-process in § 2, including the equations which govern the abundances for various sets of conditions. The present status of nuclear theory and data far from stability is presented in § 3. A first confrontation with solar system abundances is made in § 4, with the conclusion that the waiting-point approximation was valid for the conditions which produced them and that a steady flow seemed responsible for the observed abundance pattern. In § 5 we notice that the abundance pattern really requires only a stepwise steady flow between magic neutron numbers and that the *r*-process duration must have been comparable to typical beta-decay half-lives in the abundance peaks at magic neutron numbers. In addition, each of these "steps" has to result from different neutron number densities, thus finally and clearly singling out scenario 1 as the only valid choice. Section 6 focuses on the remaining uncertainties in nuclear-model predictions for the *r*-process path, which are smaller than previously but still important. In fact, the *r*-process abundance pattern seems to be able to demonstrate specific deficiencies. Section 7 discusses the astrophysical settings which could be consistent with the required conditions and how apparent earlier contradictions, inherent in scenario 1, could be overcome due to recent advances in supernova theory. Section 8 gives conclusions in a condensed form.

2. *r*-PROCESS NUCLEOSYNTHESIS

The system of differential equations for an *r*-process network includes the terms for neutron captures, neutron-induced fission, photodisintegrations, beta decays, and beta-delayed neutron emission and fission. This leads to a set of N differential equations for the individual nuclear abundances:

$$\dot{Y}(Z, A) = \sum_{Z', A'} \lambda^{Z', A'} Y(Z', A') + \sum_{Z', A'} \rho N_A \langle \sigma v \rangle_{Z', A'} Y(Z', A') Y_n , \tag{1}$$

where the first term on the right-hand side includes beta decays (with all possible emission channels, including delayed fission), spontaneous fission, and photodisintegrations. The second term includes all neutron-induced reactions. The terms are positive or negative, depending upon whether they produce or destroy the nucleus (Z, A). For the heavy (i.e., high-Z) and neutron-rich nuclei in question, only neutron-induced reactions are of importance, because of the high Coulomb barriers between the particles. Thus, only reactions involving neutrons as projectiles or emitted particles, such as (γ, n) photodisintegrations and beta-delayed neutron emission, need to be considered. The number densities n are related to the abundances Y by $n = \rho N_A Y$, where ρ is the density and N_A is Avogadro's number. Thus, we can replace $\rho N_A Y_n$ in equation (1) by n_n, underlining the fact that the number density of neutrons is the important quantity for the *r*-process rather than the neutron abundance. For nuclei with $Z < 80$, fission does not play any role, and neutron captures, photodisintegrations, and beta decays (including delayed neutron emission) dominate. If we include beta decays, leading to the emission of up to three delayed neutrons, the abundance change of nucleus (Z, A) is given by

$$\begin{aligned}\dot{Y}(Z, A) = {} & n_n Y(Z, A-1)\sigma_{A-1} + Y(Z, A+1)\lambda_{A+1} \\ & - Y(Z, A)(n_n \sigma_A + \lambda_A + \lambda_\beta^A + \lambda_{\beta n}^A + \lambda_{\beta 2n}^A + \lambda_{\beta 3n}^A) \\ & + Y(Z-1, A)\lambda_\beta^{Z-1, A} + Y(Z-1, A+1)\lambda_{\beta n}^{Z-1, A+1} \\ & + Y(Z-1, A+2)\lambda_{\beta 2n}^{Z-1, A+2} + Y(Z-1, A+3)\lambda_{\beta 3n}^{Z-1, A+3} ,\end{aligned} \tag{2}$$

where $Y(Z, A)$ is the abundance of nucleus (Z, A), n_n is the neutron number density, σ_{A-1} is the thermally averaged (n, γ) reaction rate $\langle \sigma v \rangle$ of nucleus $(Z, A-1)$, λ_{A+1} is the photodisintegration rate (γ, n) for nucleus $(Z, A+1)$, λ_β^A is the beta-decay rate of nucleus (Z, A), $\lambda_{\beta n}^A$ is the rate of beta decay followed by the emission of one delayed neutron, $\lambda_{\beta 2n}^A$ is the rate of beta decay followed by the emission of two neutrons, and $\lambda_{\beta 3n}^A$ is the rate of beta decay followed by the emission of three neutrons.

Depending upon the specific conditions, either beta decays can be faster than neutron captures and photodisintegrations as in an *s*-process, or vice versa, when an $(n, \gamma) \rightleftharpoons (\gamma, n)$ equilibrium exists. If the beta flow (i.e., the decay of the nuclei as a result of beta decays) from each Z-chain to $(Z+1)$ is equal to the flow from $(Z+1)$ to $(Z+2)$, then a steady-flow or beta-flow equilibrium will exist. When an $(n, \gamma) \rightleftharpoons (\gamma, n)$ equilibrium or a steady flow exists, equation (2) is simplified. With these simplifications a solution of the general set of equations can be avoided, which would involve a linear system of the size of the nuclear network.

As long as there is a high neutron density and a large high-energy photon density (= high temperatures), we can expect that neutron captures and photodisintegrations occur on a much faster time scale than beta decays. (This will not be the case for charged particles like protons and alpha particles, because of the large charge and Coulomb barriers of the heavy nuclei involved.) In such a case, involving large nuclear reaction rates, the small beta-decay rates can be neglected to first order and the abundance equation for the transformation of nucleus (Z, A) into $(Z, A+1)$ becomes $\dot{Y}(Z, A) = \lambda_{A+1} Y(Z, A+1) - \sigma_A Y(Z, A) n_n$. The high nuclear rates will ensure an equilibrium, i.e., $\dot{Y}(Z, A) = 0$, and an abundance ratio $Y(Z, A+1)/Y(Z, A) = (\sigma_A/\lambda_{A+1}) n_n$ in this $(n, \gamma) \rightleftharpoons (\gamma, n)$ equilibrium or waiting-point approximation, where the nucleus with maximum abundance in each isotopic chain must wait for the longer beta-decay time scale.

Reaction rates for capture and photodisintegration are related by detailed balance

$$\lambda_{A+1} = \left[\frac{2G(Z, A)}{G(Z, A+1)}\right]\left(\frac{A}{A+1}\right)^{3/2} \times \left(\frac{m_u kT}{2\pi\hbar^2}\right)^{3/2} \sigma_A \exp\left[\frac{-B_n(Z, A+1)}{kT}\right]$$

(Fowler et al. 1967), with partition functions G, the nuclear mass unit m_u, and the neutron separation (or binding) energy of nucleus $(Z, A+1)$, $B_n(Z, A+1)$, being the neutron-capture Q-value of nucleus (Z, A). This leads to abundance ratios

which are dependent only on n_n, T, and B_n:

$$\frac{Y(Z, A+1)}{Y(Z, A)} = n_n \frac{G(Z, A+1)}{2G(Z, A)} \left(\frac{A+1}{A}\right)^{3/2} \times \left(\frac{2\pi\hbar^2}{m_u kT}\right)^{3/2} \exp\left[\frac{B_n(Z, A+1)}{kT}\right]. \quad (3)$$

B_n introduces the dependence on nuclear masses, i.e., a nuclear-mass model for these very neutron-rich unstable nuclei. Under the assumption of an $(n, \gamma) \rightleftharpoons (\gamma, n)$ equilibrium, no detailed knowledge of neutron-capture cross sections is needed.

One fact which can be easily deduced from equation (3), given that $A/(A+1) \simeq 1$ and neglecting differences in the ratios of the partition functions, is that the abundance maxima in each isotopic chain are determined by the neutron number density n_n and the temperature T. Approximating $Y(Z, A+1)/Y(Z, A) \simeq 1$ at the maximum and keeping all other quantities constant, the neutron-separation energy B_n has to be the same for the abundance maxima in all isotopic chains. Figure 1 shows such a contour line of $B_n \simeq 2$ MeV for the most recent Möller et al. (1992b) mass model. In addition, it displays the line of stability and the solar r-abundances as a function of A.

The abundance flow from each isotopic chain to the next is governed by beta decays. We can introduce a total abundance in each isotopic chain $Y(Z) = \sum_A Y(Z, A)$, and each $Y(Z, A)$ can be expressed as $Y(Z, A) = P(Z, A)Y(Z)$. The individual population coefficients $P(Z, A)$ are obtained from the equilibrium condition (eq. [3]). The set of differential equations which replaces equation (2) in this case is

$$\dot{Y}(Z) = Y(Z-1) \sum_A P(Z-1, A)\lambda_\beta^{Z-1, A} - Y(Z) \sum_A P(Z, A)\lambda_\beta^{Z, A}, \quad (4)$$

where $\lambda_\beta^{Z, A}$ is the beta-decay rate of nucleus (Z, A). This is a system of as many equations as the number of Z-chains. The individual abundances are obtained from equation (3).

The waiting-point approximation is only valid for high temperatures and neutron number densities of the gas (Cameron, Cowan, & Truran 1983b). If not, the flow of nuclei toward higher neutron number N, for a given proton number Z, is steadily depleted by beta decay. As a result, only a small fraction of the flow can actually reach a waiting point. Cameron et al. (1983b) found that for temperatures of 2×10^9 K and higher, the waiting-point approximation was valid for neutron number densities as low as $n_n \simeq 10^{20}$ cm^{-3}. For lower temperatures ($T \leq 10^9$ K), even with high values of $n_n \simeq 10^{25}$ cm^{-3}, the waiting-point approximation is not valid.

When assuming a steady-flow (or beta-flow) equilibrium, in addition to an $(n, \gamma) \rightleftharpoons (\gamma, n)$ equilibrium, we also have $\dot{Y}(Z) = 0$ in equation (4), or

$$Y(Z) \sum_A P(Z, A)\lambda_\beta^{Z, A} = Y(Z)\lambda_\beta(Z) = \text{const}. \quad (5)$$

In a steady-flow equilibrium with $\dot{Y}(Z) = 0$ for each Z, the assumption of an abundance for $Y(Z_{\min})$ at a minimum Z-value is sufficient to predict the r-process curve. The calcu-

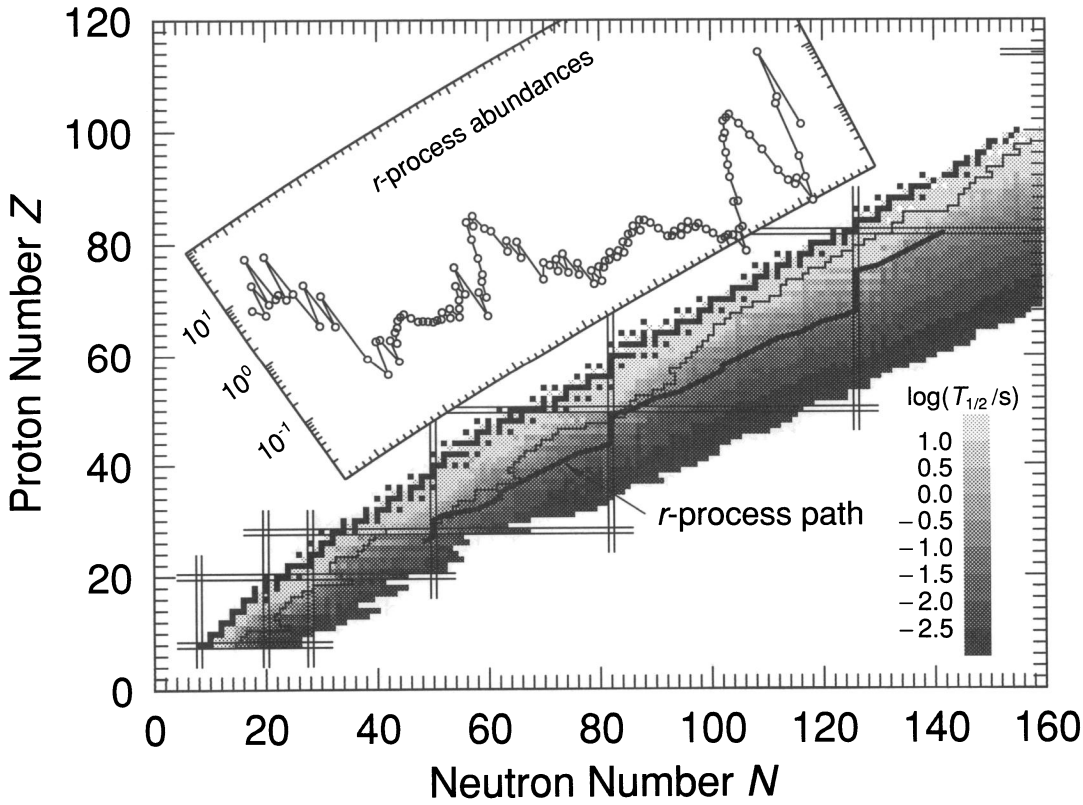

FIG. 1.—Schematic illustration of the r-process path (*dark line on neutron-rich side of beta-stability*) and observed r-abundances (*inset*). Sharp peaks occur near $A \simeq 80$, 130, and 195, where the r-process path crosses the $N = 50$, 82, and 126 magic neutron numbers. The chart of neutron-rich nucleides is shaded according to measured (near stability) and predicted beta-decay half-lives ($T_{1/2}$). Gray scales for $T_{1/2}$ ranges are explained in the legend bar.

lation of $P(Z, A)$ from equation (3) requires the knowledge of nuclear masses (or B_n values), a neutron number density n_n, and temperature T. The beta-decay rates in equation (5) are related to the half-lives of very neutron-rich nuclei via $\lambda_\beta = (\ln 2)/T_{1/2}$ (making use of the nuclear physics convention, which unfortunately can be confused with a temperature). Thus, in the simplest of all cases, i.e., provided that an $(n, \gamma) \rightleftharpoons (\gamma, n)$ equilibrium and a steady flow have been reached, the knowledge of n_n, T, nuclear masses, and half-lives alone would be sufficient to predict the whole set of abundances as a function of A. For the final decay back to stability, also beta-delayed properties (neutron emission and fission) are needed. Recent results by Kratz et al. (1988b, 1990, 1991a) seemed to indicate that this should be the case in order to reproduce the solar system r-process abundances, at least locally in the $A \simeq 80$ and $A \simeq 130$ peak regions. We will discuss this in more detail in §§ 4 and 5.

3. NUCLEAR DATA

3.1. *General Considerations*

The observed isotopic r-abundances are the result of successive neutron captures along the r-process path and decay back to beta stability, thus depending—apart from stellar parameters—on nuclear properties of nuclei with extreme N/Z ratios. In the general case, as discussed with equation (2), among nuclear properties, ground-state masses (resp. Q_β values), neutron-separation energies (B_n), beta-decay half-lives ($T_{1/2}$), probabilities of beta-delayed neutron emission (P_n), neutron-capture cross sections ($\sigma_{n,\gamma}$), and ground-state spins (J^π) are of paramount importance in r-process calculations. For nuclei with $Z \geq 80$, fission barriers and rates of beta-delayed as well as neutron-induced fission are also important. Since the vast majority of nuclei in or close to the r-process path is not accessible in terrestrial laboratories, a general understanding of their nuclear structure properties may only be obtained through theoretical means. In fact, only within the last few years has it been possible to measure the $T_{1/2}$ and P_n values of the first nuclei in the bends of the r-process path at the magic neutron numbers $N = 50$ and $N = 82$, where the r-process path comes closest to beta-stability, i.e., ^{79}Cu, ^{80}Zn, and ^{130}Cd (Ekström et al. 1986; Gill et al. 1986; Kratz et al. 1986, 1991a, b; see also Table 1 of this paper). This situation presents a continuing, stimulating challenge to both theoreticians and experimentalists in the nuclear physics community. Neutron-capture cross sections can be calculated with the statistical model (Hauser-Feshbach), as long as nuclear level densities in the compound nucleus are sufficiently high to justify such an approach. This method requires the knowledge of the relevant physics quantities (e.g., optical potentials, giant dipole resonance parameters for gamma widths, level-density parameters, reaction Q-values B_n) either from experiment (for level densities of neutron-rich isotopes see, e.g., Kratz et al. 1983; Kratz & Thielemann 1988) or from theory (Thielemann, Arnould, & Truran 1987; see also § 3 in Cowan et al. 1991a). For nuclei near closed neutron shells, the level density is smaller and the Hauser-Feshbach approach might not be applicable and should be replaced by Breit-Wigner resonance-capture plus radiative-capture contributions (Mathews et al. 1983). When one considers a steady-flow r-process, whose path is not determined by the neutron-capture cross sections, the important properties are only B_n, $T_{1/2}$, and P_n.

Before proceeding with a detailed discussion, we would first like to point out a fact which might sound trivial but is critical. Since a number of different quantities are needed in r-process calculations, in the past it was not possible to obtain them all from one source. Taking them from different sources, however, raises the question of consistency. Fission barrier height predictions reflect properties of the specific mass model employed. Beta-decay half-lives reflect mass differences (or Q_β values). Thus, it is inconsistent to mix specific mass models for predicting B_n and the r-process path, with fission barriers and half-lives originating from different approaches. In such mixed calculations, although often done in the past because of the lack of data (see, e.g., Cowan et al. 1991a), occasionally nuclear structure effects may vanish or "artificial" effects may show up, thus strongly limiting the predictive power far off beta stability.

3.2. *A Unified Approach*

In light of the above, the approach to nuclear structure calculations applied in the present paper is a unified one as outlined by Möller et al. (1990, 1992a), who used a theoretical framework within which all of the above-mentioned nuclear properties can be studied in a "self-consistent" way. The results are obtained in the macroscopic-microscopic approach (Strutinski 1967, 1968; Nix 1972). A microscopic nuclear structure single-particle model with extensions is combined with a macroscopic model, such as the liquid-drop model. In this model the total potential energy of the nucleus may be calculated as a function of shape. The maxima and minima in this function correspond to such features as the ground state, fission saddle point, and shape-isomeric states. Various transition rate matrix element (i.e., for beta decay) are determined from wave functions calculated in the single-particle model with pairing and other relevant residual interactions taken into account.

As a first step in calculating nuclear structure properties of interest in astrophysical studies, it is natural to determine nuclear ground-state masses and shapes. Once these quantities are known, nuclear wave functions may be calculated for the appropriate shapes. Matrix elements giving beta-decay transition rates and any other quantities of interest may then be determined.

Ground-state masses were taken from the most recent version of the finite-range droplet model (Möller et al. 1992b), which includes Coulomb redistribution effects (Möller et al. 1992a) and an improved formulation of the pairing model (Möller & Nix 1992). This model has its origin in the 1981 mass model (Möller & Nix 1981) which utilized the folded Yukawa single-particle potential (Bolsterli et al. 1972; Möller & Nix 1974). The model used in the current calculations will be completely specified in a forthcoming contribution to Atomic Data and Nuclear Data Tables (Möller et al. 1992b). When the model parameters were determined only from nuclear masses known until 1981 and then applied to "predict" the 350 new masses far from stability obtained since then, the errors did not increase in comparison with the original data set. This is a strong reliability test for this new model (see Möller et al. 1992a). Its errors were found to be considerably smaller than those for the models of Truran, Cameron, & Hilf (1970) and Hilf, von Groote, & Takahashi (1976) so far used in astrophysical calculations. It has already been pointed out by Cowan et al. (1991a) that other droplet model versions, such as, e.g., Myers (1976) and von Groote, Hilf, & Takahashi (1976) showed increasing deviations from experimental masses with

increasing distance from the valley of stability and should not be used for such purposes.

Beta-decay properties, $T_{1/2}$ and P_n, were deduced from theoretical Gamow-Teller (GT) strength functions. The quantity of a beta-strength function corresponds to the energy distribution of the reciprocal *ft*-value (Duke et al. 1970) and is usually defined in terms of the reduced GT transition probability

$$B'(GT) = 6260(g_v/g_A)^2/ft \ . \quad (6)$$

With this concept, the beta-decay half-life is connected to the GT strength function by the expression

$$1/T_{1/2} = \sum_{0<E_i<Q_\beta} B'_i(GT) f(Z, Q_\beta - E_i) \ , \quad (7)$$

summed over all excited states in the daughter nucleus, where $f(Z, Q_\beta - E_i)$ is the Fermi function. With this definition, $T_{1/2}$ yields information on the average beta feeding of a nucleus. However, the low-energy part of its excitation spectrum is strongly weighted because of the energy factor of beta decay $f(Z, Q_\beta - E_i) \propto (Q_\beta - E_i)^5$. The quantity $T_{1/2}$ is thus predominantly determined by the lowest energy nuclear structures in the GT strength function (see, e.g., Kratz 1984).

The beta-delayed neutron emission probability P_n, is schematically given by

$$P_n = \sum_{B_n<E_i<Q_\beta} [B'_i(GT) f(Z, Q_\beta - E_i)] \Big/ \sum_{0<E_i<Q_\beta} [B'_i(GT) f(Z, Q_\beta - E_i)] \ , \quad (8)$$

when assuming that neutron emission wins always over gamma transitions above the neutron binding energy B_n. This defines P_n as the ratio of the integral beta feeding to neutron-unbound states and the total beta intensity. Again, because of the E_β^5 dependence of the Fermi function, the P_n value is mainly determined by the nuclear structures just beyond the neutron binding energy.

In the framework of our *unified* approach we have calculated the GT strength functions within the quasi-particle random-phase approximation (QRPA), using the same folded Yukawa single-particle levels as for the shell corrections of the nuclear masses. The ground-state shapes determined in the mass calculations were used to determine the configurations of mother and daughter nuclei in the GT beta-strength calculations. The present QRPA model (Möller & Randrup 1990) represents an extension of earlier work on beta-strength functions by Hamamoto (1965), Halbleib & Sorenson (1967) and Krumlinde & Möller (1984). It uses a deformed single-particle model, here the folded Yukawa model (for certain applications the Nilsson or Woods-Saxon models can also be chosen), to obtain the energies and wave functions that serve as the starting point for calculating the initial state in the mother and the final state in the daughter nucleus. Pairing is treated in the Lipkin-Nogami approximation (again, for certain applications different versions of the BCS model can also be used). To account for the retardation of low-energy GT decay rates, as in the 1984 Krumlinde-Möller model, a simple residual interaction specific to GT decay is added to the Hamiltonian. This residual interaction is studied in the quasi-particle random-phase (QRP) approximation. Recently, Klapdor and collaborators (Staudt et al. 1989, 1990) adopted the deformed QRPA model of Krumlinde & Möller (1984) in a practically identical formulation. However, there are significant differences in how the Klapdor group and our group obtain the parameters used in the respective calculations. Whereas we use for the GT coupling constant χ_{GT} the value $23/A$ MeV throughout the periodic system, Staudt et al. (1990) choose for each individual isotopic chain with charge Z a different value, for which the model optimally reproduces the *known* beta-decay half-lives. In our opinion, not only does this lead to an excessive number of "unphysical" model parameters, but also one gives up the ability to identify nuclear structure signatures causing deviations, which might not be only Z-dependent.

In principle, with the above *unified* approach, for the first time a *consistent* nuclear data set for astrophysical calculations is available which is expected to yield more reliable predictions of nuclear physics parameters than earlier models. Nevertheless, being aware that this new approach also must have its deficiencies, we have further improved our nuclear physics data set by also including in the beta-strength function calculations first-forbidden transitions modeled as in the Gross theory (Takahashi, Yamada, & Kondo 1973) and by taking into account recent experiments (up to 1991 December) as well as known nuclear structure properties, either (model-inherently) not contained or incorrectly described by our above still too simplistic approach. In the following we will give a few examples.

3.3. *Remaining Deficiencies*

The QRPA model for calculating GT strength functions in its present form assumes identical ground-state deformations for mother and daughter nuclei (Möller & Randrup 1990). Hence, beta decays between isobars of different nuclear shape, e.g., an oblate mother decaying into a prolate daughter, as well as (most) cases of shape coexistence in the final nucleus, cannot be described in a correct way (see, e.g., Kratz 1988; Kratz et al. 1989; Möller et al. 1990). In consequence, our theoretical beta-strength functions will be "wrong" and also the deduced $T_{1/2}$ may be wrong—or only "correct" by chance. Hence, we will have to expect that errors in calculated half-lives up to an order of magnitude may also occur occasionally when the model is applied to unknown regions of nuclei.

Other examples are related to the missing monopole and quadrupole proton-neutron interactions in the present QRPA model. These residual interactions play an important role in the development of nuclear structure in transitional regions, e.g., near $A = 100$ (for a survey see Eberth, Meyer, & Sistemich 1988). The monopole part defines and modulates the energies of the single-particle states (e.g., with the filling of the $1g_{9/2}$ proton shell, the $1g_{7/2}$ neutron orbitals are lowered) that form the configuration space within which the quadrupole part generates collectivity. This interplay leads to the well-known rapid phase transition between spherical and strongly deformed ground-state shapes in the neutron-rich $A \simeq 100$ region. The neglect of the proton-neutron interactions in our QRPA model manifests itself, for example, in an underestimation of the spherical $N = 56$ subshell strength and in a too early (smooth) onset of deformation over a too wide Z-range (Möller & Nix 1981; Möller et al. 1992b). This behavior has initiated recent experimental studies in the region around $^{92}_{36}Kr_{56}$ (Kratz et al. 1988a; Neugart et al. 1988; Wöhr et al. 1991, 1992). As an example, Figure 2 shows two theoretical GT strength functions for $^{93}_{35}Br_{58}$ (the heaviest known odd-mass Br isotope), one with the predicted prolate deformation (Möller at al. 1992b) and the other with spherical shape which corresponds to the recent experimental findings. The observation of substantial differences in the calculated $T_{1/2}$ and P_n values reflects a fortunate

aspect of nuclear physics, i.e., that for nuclei far from stability often the most important structure information (i.e., nuclear shape or collectivity) can already be obtained from easily measurable quantities, such as the first 2^+ states in even-even nuclei or the $T_{1/2}$ and P_n values.

With this, an identification of deviations of predicted nuclear structure properties from experimental ones may serve as a local basis for more reliable extrapolations to unknown neighboring isotopes or isotones. In our model this can be achieved through a change of certain parameters, e.g., quadrupole deformation or single-particle energies of specific orbits. However, one should again have in mind that such convenient parameter changes can usually not be invoked when the QRPA model is applied to completely unknown regions of nuclei.

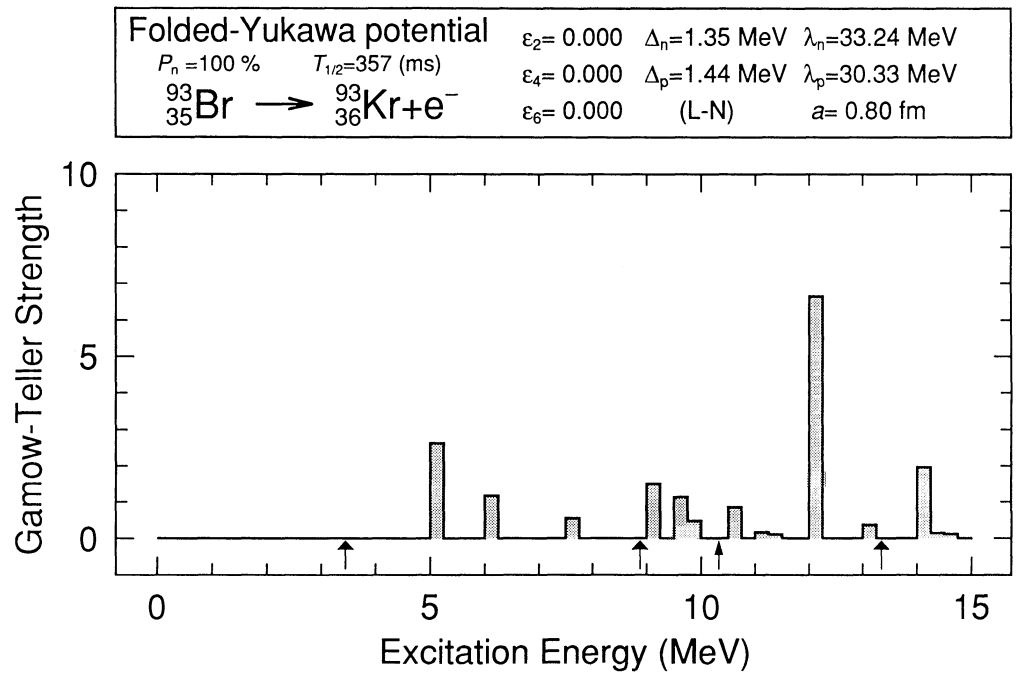

FIG. 2*a*

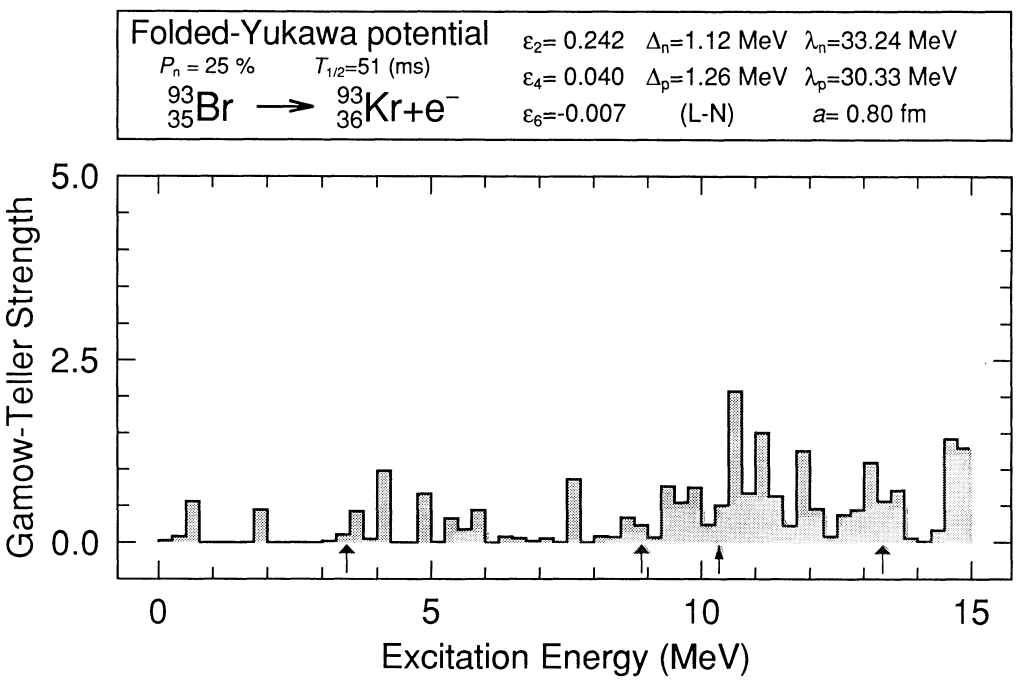

FIG. 2*b*

FIG. 2.—(*a*, *b*) Gamow-Teller (GT) strength functions for ^{93}Br decay obtained from QRPA calculations using the folded Yukawa single-particle potential, the Lipkin-Nogami pairing, and two different assumptions for the value of quadrupole deformation indicated by ϵ_2, ϵ_4, and ϵ_6.

Another aspect in the discussion of residual interactions concerns the shell strength far from stability, in particular in the astrophysically interesting regions around the doubly magic isotopes $^{78}_{28}Ni_{50}$ and $^{132}_{50}Sn_{82}$. As an example, we show in Figure 3 a comparison of the experimental level scheme of ^{80}Ga from Ekström et al. (1986)—which is in its main features identical to that published by Winger et al. (1987)—with our QRPA predictions for spherical and deformed shapes (Kratz et al. 1988a). The key result of this comparison is that the lowest-lying $J^\pi = 1^+$ states in ^{80}Ga can only be reproduced when assuming the beta-decay daughter to be deformed, at least above 600 keV. The observed splitting of the spherical 2QP 1^+ states, as well as the reasonable agreement of theoretical log ft values, $T_{1/2}$ and P_n with experiments (Ekström et al. 1986; Winger et al. 1987; Kratz et al. 1991b) strongly suggests that also the ground state of the mother isotope $^{80}Zn_{50}$ is prolate, and *not* spherical as one might expect in the close vicinity of ^{78}Ni (Möller et al. 1992b). This implies a rather rapid weakening of the shell strength above ^{78}Ni, similar to what has been observed below ^{132}Sn.

Again, for nearby extrapolations this effect can be taken into account in our QRPA calculations by adopting the experimental trends in the decrease of deformation when approaching $N = 50$ (see, e.g., the sequence of Zn isotopes in Ekström et al. 1986) or $N = 82$ (see here the sequences of the Cd and In isotopes, e.g., in the Proceedings of the Fifth Conference on Nuclei Far from Stability; Towner 1988). However, we do not know to what extent the strengths of the $N = 82$ and $N = 126$ shells still influence extremely neutron-rich r-process isotopes below and beyond the magic neutron number waiting-point nuclei with $45 \leq Z \leq 50$ and $64 \leq Z \leq 70$. In these regions, a priori we will have to "believe" our model predictions. When discussing the deviations of our calculated isotopic r-process abundances from observed values in § 6, we will come back to this important question about shell strengths far from stability.

Summarizing this part, we believe that with our *unified* approach described above (see also Möller et al. 1992a), together with the inclusion of measured $T_{1/2}$ and P_n values as well as local improvements of the QRPA calculations due to experimental knowledge of nuclear structure far from stability included in the $T_{1/2}$ table of Pfeiffer, Möller, & Kratz (1991), we have the best data set of nuclear physics parameters for astrophysical calculations presently available. Nevertheless, we are aware of the fact that even this data base is still far from perfect. Therefore, deviations will be appreciated as possible signatures of nuclear structure.

4. FIRST CONSTRAINTS FROM SOLAR ABUNDANCES

It is worthwhile to ask whether the isotopic abundance patterns in the solar r-process composition, together with our knowledge of nuclear properties, can give a clue to the r-process conditions. Because of recent experimental and theoretical efforts in regions around $A \simeq 80$ (magic neutron number $N = 50$) and $A \simeq 130$ ($N = 82$), where the r-process

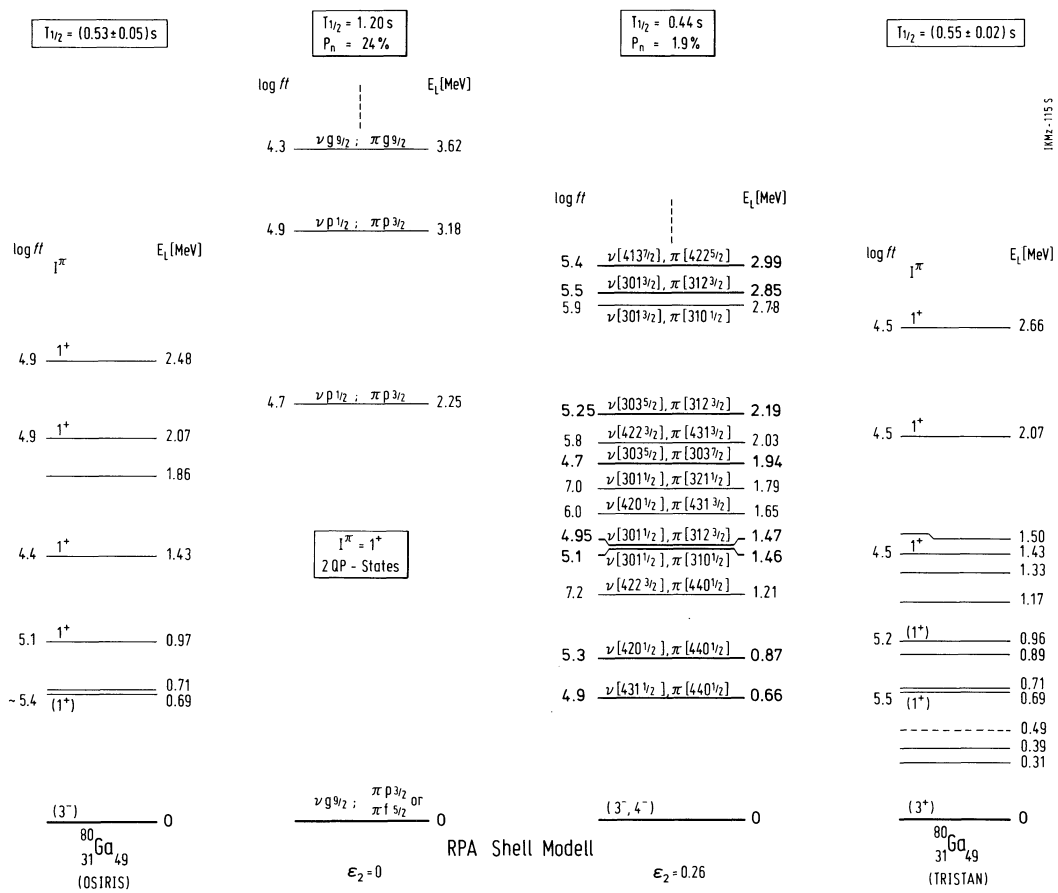

FIG. 3.—Comparison of the measured half-life ($T_{1/2}$) and decay scheme of ^{80}Zn (Ekström et al. 1986; Winger et al. 1987) with QRPA shell-model predictions for two different values of the quadrupole deformation (Kratz et al. 1988a).

path comes closest to stability, it is most appropriate to focus on the abundance patterns in both of these *r*-process peaks.

Beta-delayed neutron emission has an impact on the final shaping of the isotopic abundances during the beta decays back to stability, after the *r*-process freeze-out of an $(n, \gamma) \rightleftharpoons (\gamma, n)$ equilibrium at low n_n and T. Figures 2 and 3 in Kratz et al. (1988b) summarize the information in the $N = 50$ and $N = 82$ regions, especially with respect to P_n values. With this information it is possible to predict the isotopic ratios of the final stable nuclei after decay, provided that one knows the location of the *r*-process path as well as the abundances of progenitor nuclei in the path.

In Kratz et al. (1988b) we made the working hypothesis that the *r*-process abundances are produced under conditions of an $(n, \gamma) \rightleftharpoons (\gamma, n)$ equilibrium. In such a case, for a number of *Z*-values at the neutron magic numbers $N = 50$ and $N = 82$, only one isotope contains the dominant abundance with $N = N_{\text{magic}}$. Neutron number densities and temperatures for which the $N = 82$ isotones ^{127}Rh, ^{128}Pd, ^{129}Ag, and ^{130}Cd *as well as* the $N = 50$ isotones ^{77}Co, ^{78}Ni, ^{79}Cu, and ^{80}Zn possess the maximum abundances in their isotopic chains are shown in Figure 4 as a shaded area within the solid lines. This is the intersection of Figures 2 and 3 in Kratz et al. (1988b). At a maximum *Z*, the *r*-process finally branches off from the magic neutron number and two even-*N* isotopes share the dominant abundance. In this way, the isotopic ratios of ^{131,133}In and ^{81,83}Ga are related to the abundances of the stable isotopes ^{131,132}Xe and ^{81}Br and ^{83}Kr, respectively. The beta-delayed neutron emissions of ^{133}In and ^{83}Ga play an important role in these ratios, and are both experimentally determined. The n_n-T conditions necessary to reproduce the ^{81,83}Ga and ^{131,133}In isotopic abundance ratios (using two different mass formulae; Hilf et al. 1976 and Möller & Nix 1981) form lines which are also located within the shaded area. The additional (thick) line beyond which the neutron-capture and photodisintegration time scales $\tau_{n,\gamma}$ and $\tau_{\gamma,n}$ are shorter than $\tau_\beta = 1/\lambda_\beta$ marks the boundary where the waiting-point approximation is valid and an $(n, \gamma) \rightleftharpoons (\gamma, n)$ equilibrium attained (Cameron et al. 1983b).

These findings, showing that in an $(n, \gamma) \rightleftharpoons (\gamma, n)$ equilibrium the *r*-process peaks can be produced at the right locations for conditions which also reproduce key isotopic features, suggested that the solar *r*-process abundances were, indeed, produced under conditions consistent with the waiting-point approximation. Although the region is quite broad, the requirements for the $A \simeq 80$ and $A \simeq 130$ abundance peaks seemed very similar. We interpreted this to mean that, within the still existing nuclear uncertainties, the conditions for both mass regions are identical. The area close to the intersection of the n_n-T band and the thick line would represent freeze-out conditions which gave the final imprint to solar *r*-process abundances in cooling and expanding material.

One can perform an additional test. In an $(n, \gamma) \rightleftharpoons (\gamma, n)$ equilibrium close to the $A \simeq 80$ and $A = 130$ peaks, only one nucleus dominates each isotopic chain. When assuming that we also have a steady-flow (or beta-flow) equilibrium, the sum over A in equation (5) is reduced to one term at $N = 50$ or $N = 82$. In such a case, we find $Y(Z)\lambda_\beta(Z) \propto Y(Z)/T_{1/2}(Z) =$ constant along the magic neutron numbers. From the known abundances of stable isotopes and known P_n values for beta-delayed neutron emission, one can predict the abundances of the progenitor isotopes in the *r*-process path, and therefore also "predict" the beta-decay half-lives for these nuclei, with the aid of equation (5). Table 1 indicates that the half-lives

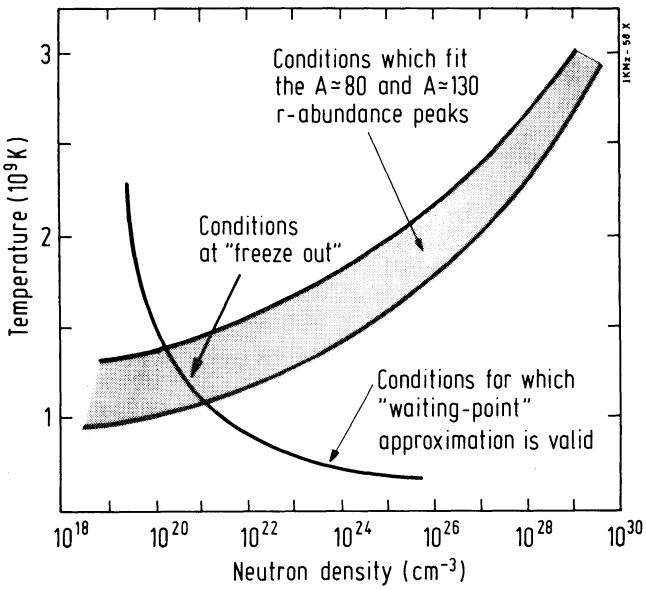

FIG. 4.—Neutron number densities n_n and temperatures T_9 consistent with observed *r*-process peaks (Käppeler, Beer, & Wisshak 1989) and measured beta-decay rates (Kratz et al. 1988b). Also shown are the conditions found by Cameron, Cowan, & Truran (1983b) for which the classical waiting-point approximation is valid (*beyond solid line*). The thick arrow illustrates temperatures and densities in an *r*-process environment before freeze-out at $n_n \simeq 10^{20}$ cm^{-3} and $T \simeq 10^9$ K.

predicted in such a way agree closely with experimental or QRPA values (Kratz 1988; Kratz et al. 1991b), thus also suggesting that a beta-flow or steady-flow equilibrium was achieved. It is worth mentioning in this context that our new data on ^{79}Cu ($T_{1/2}$, P_n) and the low P_n value of ^{80}Zn (Kratz et al. 1991a) agree closely with the earlier QRPA predictions (Kratz et al. 1988a, b), thus further strengthening these arguments.

When accepting the above implications for the neutron closed-shell nuclei at $A \simeq 80$ and $A \simeq 130$, one can also predict the progenitor abundances and the solar *r*-process abundances

TABLE 1

EXPERIMENTAL VERSUS MODEL-PREDICTED HALF-LIVES[a]

ISOTOPE	BETA-DECAY HALF-LIFE $T_{1/2}$ (ms)		
	Experiment	QRPA	Beta Flow
^{83}Ga	308 ± 1	235	...
^{81}Ga	1221 ± 5	1365	...
^{80}Zn	537 ± 29	420	750
^{79}Cu	188 ± 25	195	200[a]
^{78}Ni	...	210	185[a]
^{77}Co	...	10	≤11.5[a]
^{135}In	195 ± 3	170	...
^{131}In	278 ± 3	285	...
^{130}Cd	195 ± 35	170	180
^{129}Ag	...	140	160
^{128}Pd	...	115	140
^{127}Rd	...	70	100

NOTE.—Comparison of experimental beta-decay half-lives of $N \simeq 50$ and $N \simeq 82$ isotopes in the *r*-process path with predictions from our QRPA shell model (Pfeiffer, Möller, & Kratz 1991) and from the astrophysical requirement of a beta-flow equilibrium (Kratz et al. 1988b; Kratz 1988).

[a] Normalized to experimental $T_{1/2}(^{80}\text{Zn})$.

in between magic neutron numbers (after correcting for beta-delayed neutron branching during decay back to stability). As a first test we chose the mass region $90 \leq A \leq 100$ for two reasons: (1) the stellar origin of ^{96}Zr is of special interest in connection with the recently observed correlated ^{50}Ti–^{96}Zr isotopic anomalies in several EK-inclusions of the Allende meteorite (Harper et al. 1990), and (2) ^{100}Mo is an *r*-only isotope, which can—if necessary—be used for an absolute normalization of the calculated *r*-abundances to the observed ones (Käppeler, Beer, & Wisshak 1989). A schematic view of the *r*-process path at freeze-out conditions ($T_9 \simeq 1.0$; $n_n \simeq 10^{20}$ cm^{-3}) and the *r*-abundance features in the $90 \leq A \leq 100$ region is shown in Figure 5. The most interesting result is that we calculate *r*-abundances in fair agreement with the observed solar values for the whole region. This is most evident from the simultaneous reproduction of the abundance of the *r*-only isotope ^{100}Mo and the solar *r*-contribution to ^{99}Tc, which both originate from the same progenitor isotope ^{100}Kr. Another important result is that for these n_n-T conditions ^{96}Zr would also be an *r*-only isotope, mainly produced from beta-delayed neutron emission of ^{97}Br.

Thus, we tested the predictions of a model based on the waiting-point approximation and a steady flow in three areas, around $A \simeq 80$ and $A \simeq 130$ and for $90 \leq A \leq 100$ and found good agreement. This is accumulated evidence that the solar *r*-process abundances originated from freeze-out abundances of an *r*-process with conditions within the shaded area of Figure 4, thus attaining an $(n, \gamma) \rightleftharpoons (\gamma, n)$ equilibrium. This indicates $n_n \geq 10^{20}$ cm^{-3} and $T \geq 10^9$ K. Apparently, a steady-flow equilibrium was also established. This excludes scenario 2, discussed in § 1 (i.e., explosive He-burning environments). It should be mentioned here that such environments also experienced other difficulties, in particular insufficient neutron production via (α, n) reactions in realistic stellar conditions (Blake et al. 1981; Cowan, Cameron, & Truran 1985).

In a continuation of this effort, the whole region $80 \leq A \leq 130$ was attacked with the same conditions which reproduced the ^{131,132}Xe isotopes and the $90 \leq A \leq 100$ areas nicely. We calculated the abundances in the *r*-process path according to equations (3) and (5), normalizing $Y(Z)\lambda_\beta(Z)$ or equivalently $Y(Z)/T_{1/2}(Z)$ to the closed neutron-shell isotope ^{130}Cd, which is the only abundant isotope in its respective Z-chain. In the $A = 130$ isobaric chain, beta-delayed neutron branching is so small that one can assume a one-to-one correspondence between the original abundance of the progenitor nucleus in the *r*-process path and the final *r*-abundance of its stable decay product ^{130}Te. Then normalization to solar *r*-abundances led to $Y(Z)/T_{1/2}(Z) \simeq 11.5$ s^{-1} (using not the

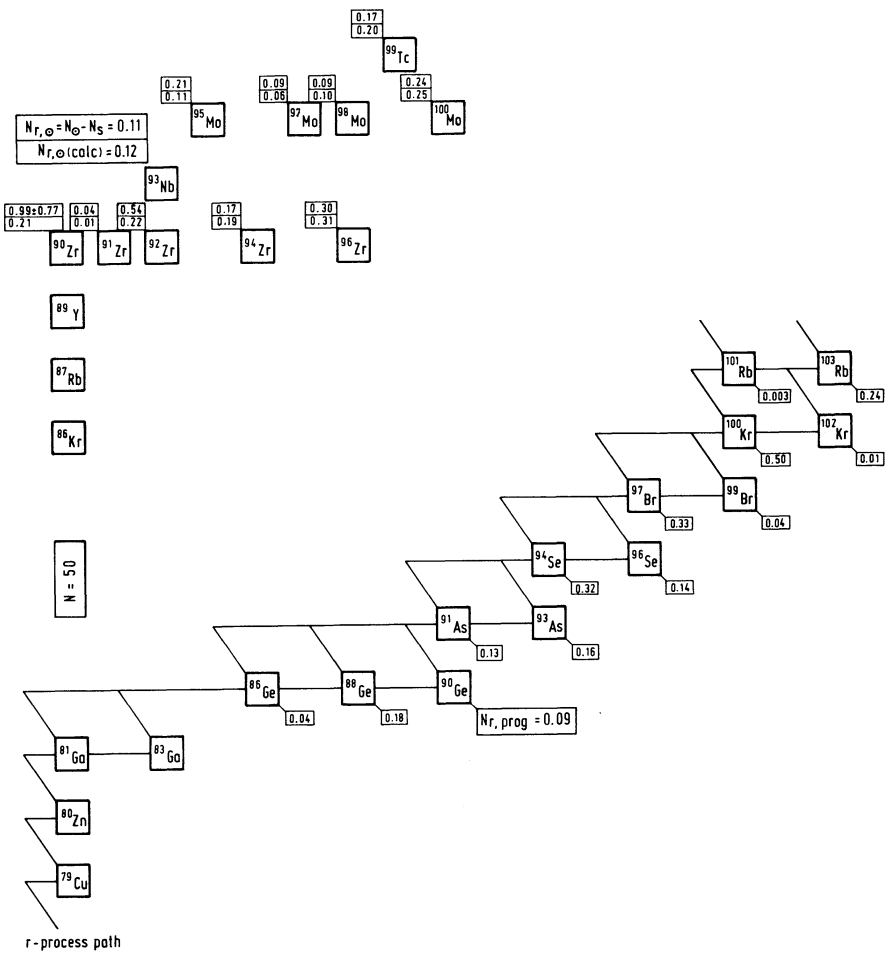

FIG. 5.—Schematic view of the *r*-process path at freeze-out conditions and *r*-abundance features in the $90 \leq A \leq 100$ mass region. Applying an $(n, \gamma) \rightleftharpoons (\gamma, n)$ and steady-flow equilibrium, abundances $[N_{r,\odot}(\text{calc})]$ after beta decay and delayed neutron emission are derived for stable isotopes from ^{90}Zr to ^{100}Mo. These abundances are in fair agreement with the observed values ($N_{r,\odot}$, from Käppeler et al. 1989) when normalizing to ^{130}Cd, but *not* to ^{80}Zn.

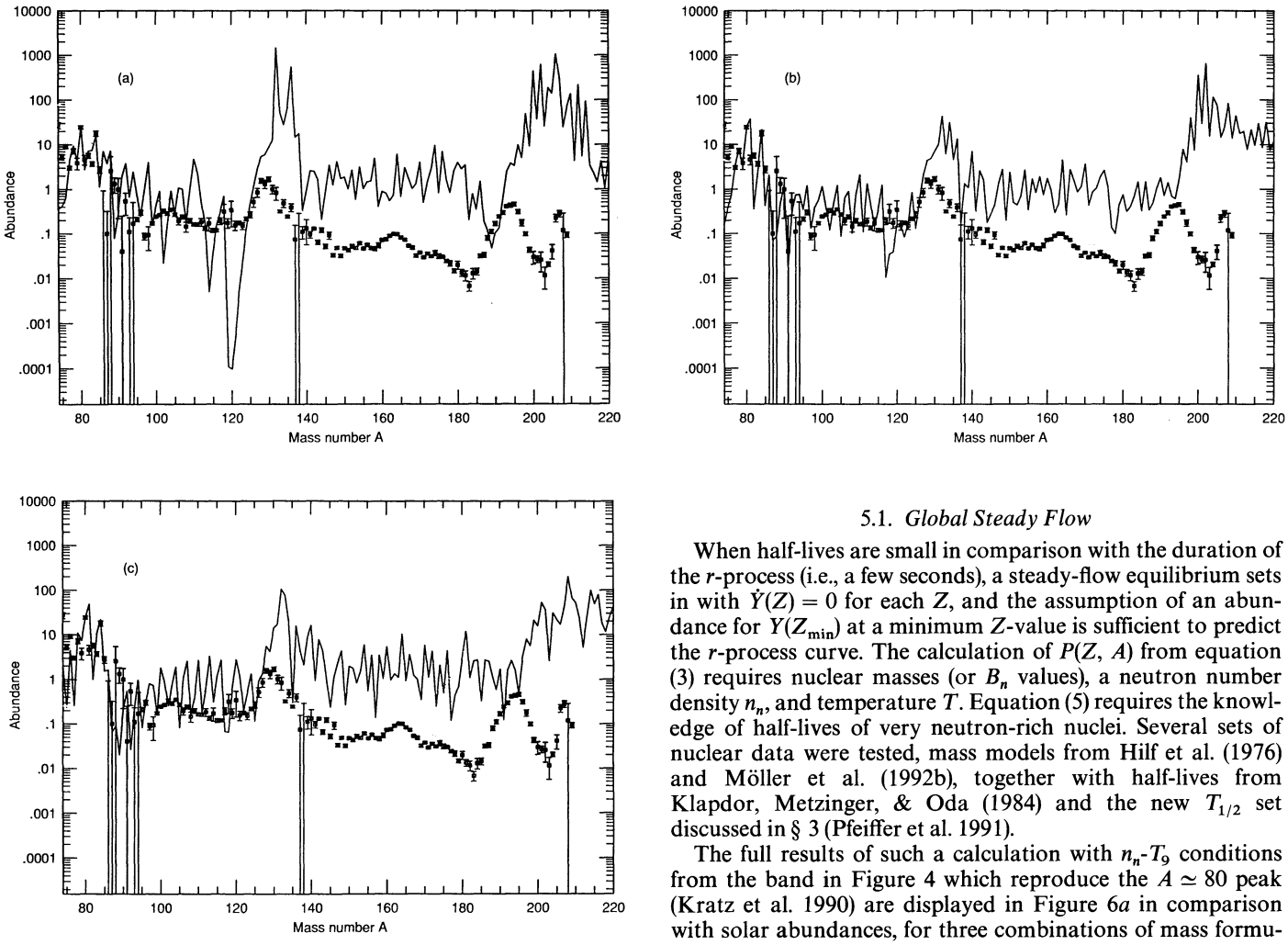

FIG. 6.—Global r-abundance curves, after beta decay, obtained using the waiting-point and steady-flow approximation with $T_9 = 1.3$ and $n_n = 10^{20}$ cm^{-3}. The small open squares with error bars represent the solar r-process abundances (Käppeler et al. 1989): (*a*) r-process calculations using the Möller et al. (1992b) mass model and the $T_{1/2}$ and P_n values from the Pfeiffer, Möller, & Kratz (1991) set; (*b*) same as (*a*), but using the Hilf, von Groote, & Takahashi (1976) masses: (*c*) same as (*a*), using the Hilf et al. (1976) masses and half-lives and P_n values from Klapdor, Metzinger, & Oda (1984).

normal definition of Y but the shifted scale which sets an abundance of 10^6 for ^{28}Si). While this resulted in an excellent fit for $90 \leq A \leq 130$, the $A \simeq 80$ region was underproduced, requiring a normalization of 43.5 s^{-1} instead. This is a first grain of salt for a *global* steady-flow equilibrium over the whole r-process path. In § 5 we will scrutinize this finding in more detail.

5. FIT TO SOLAR r-ABUNDANCES

Here we want to generalize the tests for the whole set of r-process abundances, which in § 4 were performed for selected regions only. In particular, we will focus on the question whether the steady-flow manifestations for $A \simeq 80$ and $A \simeq 130$ and for $90 \leq A \leq 100$ can be verified to be part of a global steady flow, or form only local components. In addition, it shall be shown how time-dependent calculations can reproduce steady-flow patterns and solar abundances.

5.1. *Global Steady Flow*

When half-lives are small in comparison with the duration of the r-process (i.e., a few seconds), a steady-flow equilibrium sets in with $\dot{Y}(Z) = 0$ for each Z, and the assumption of an abundance for $Y(Z_{\min})$ at a minimum Z-value is sufficient to predict the r-process curve. The calculation of $P(Z, A)$ from equation (3) requires nuclear masses (or B_n values), a neutron number density n_n, and temperature T. Equation (5) requires the knowledge of half-lives of very neutron-rich nuclei. Several sets of nuclear data were tested, mass models from Hilf et al. (1976) and Möller et al. (1992b), together with half-lives from Klapdor, Metzinger, & Oda (1984) and the new $T_{1/2}$ set discussed in § 3 (Pfeiffer et al. 1991).

The full results of such a calculation with n_n-T_9 conditions from the band in Figure 4 which reproduce the $A \simeq 80$ peak (Kratz et al. 1990) are displayed in Figure 6*a* in comparison with solar abundances, for three combinations of mass formulae and half-lives. They do produce three r-abundance peaks; however, there exist major problems. The $A \simeq 130$ and $A \simeq 195$ peaks are much taller than they should be and are also shifted to the right, which means that n_n is too low. This seems at first glance to be in contradiction to our earlier findings. However, in § 4 we noticed the need for different normalizations of the $A \simeq 80$ and $A \simeq 130$ peaks. A very important feature of the above calculation is that the height of the peaks is *rising* with A, in contrast to earlier steady-flow calculations (Cameron et al. 1983a).

In order to verify whether this might only be a flaw of one particular nuclear data set, we repeated this procedure also for the mass model of Hilf et al. (1976) with our set of half-lives and those of Klapdor et al. (1984). The results are displayed in Figures 6*a*, 6*b*, and 6*c*, and show the same general behavior, although different in details. In neither case was it possible to obtain an abundance curve decreasing with increasing A.

The question arises, how can this be reconciled with the results by Cameron et al. (1983a)? There are two possible reasons: either (1) very different properties of the mass formula by Truran et al. (1970) were employed in those studies, or (2) Cameron's findings result from a steady flow but without $(n, \gamma) \rightleftharpoons (\gamma, n)$ equilibrium. Cameron et al. performed these steady-flow calculations with $n_n = 10^{20}$ cm^{-3}, but $T_9 = 0.3$–0.6. Under such conditions, photodisintegrations are negligible and a steady flow is characterized by the competition of

neutron captures and beta decays. If this leads to an increasingly more neutron-rich r-process path for heavier nuclei, due to increasing neutron-capture cross sections (with A), the encountered beta-decay half-lives will be shorter accordingly. They, however, are proportional to the abundances in a steady flow. Decreasing half-lives (on average) with increasing A along the r-process path would lead to decreasing abundances. This makes the difference between our steady-flow calculations and the ones by Cameron et al. (1983a) understandable, but also excludes—together with our findings from § 4—their solution as a possible one. Thus, we come to the conclusion that the solar r-process abundances, with declining peak heights as a function of A, cannot be explained by a global steady flow with $(n, \gamma) \rightleftharpoons (\gamma, n)$ equilibrium.

On the other hand we noticed in § 4 that individual regions are well represented by a steady flow with $(n, \gamma) \rightleftharpoons (\gamma, n)$ equilibrium. We now have to investigate systematically what the (probably different) conditions are which reproduce these regions well and where the break points are located which prohibit a global steady flow. Finally, we have to understand in which framework the different regions can be joined.

5.2. *Reproducing Individual r-Process Regions*

In a first attempt to overcome the problems encountered in a global steady-flow assumption, we will focus now on reproducing the details of individual regions and finding the break points between steady-flow areas. First we will have a look at r-process peaks. We consider a range of about 10 mass numbers A around the peak position and search for a minimum of the quantity

$$\epsilon = \sum_A \{\log [Y(A)_{\rm calc}/Y(A)_{\rm obs}]\}^2$$

as a function of neutron number density n_n and temperature T_9. In the $A \simeq 80$ peak, two isotopes are especially abundant, ^{80}Se and ^{84}Kr. A best fit was obtained for a neutron number density around $n_n = 2.67 \times 10^{20}\text{cm}^{-3}$ and $T_9 = 1.35$. In Figures 7*a* and 7*b* we display results in comparison with solar abundances, (*a*) in the r-process path before beta decay and (*b*) after beta decay back to stability. The (improving) effect of beta-delayed neutron emission is easily recognizable. The fit is very good for $77 \leq A \leq 85$. No choice of n_n gave a good fit beyond $A = 85$ and below $A = 77$. We will return to these points in a later discussion.

For the $A \simeq 195$ peak we obtained a best fit with $n_n = 3.0 \times 10^{22}$ cm^{-3} and $T_9 = 1.2$, which requires a neutron density higher by two orders of magnitude (see Fig. 8). The main reason is the location of the $A \simeq 195$ peak. Smaller neutron densities would result in an r-process path closer to stability and a peak maximum at a larger mass number A. As in the case of the $A \simeq 80$ peak, the quality of the fit is worse after the maximum and overproduces nuclei by factors of 10–100. Thus, it is obvious that in the right wing of each peak the agreement becomes poorer, indicating that beyond the abundance maxima the steady-flow approximation becomes invalid.

This is easily understandable. In the abundance maxima, i.e., at the upper end of the kinks in the r-process path at magic neutron numbers, the r-process experiences the longest half-lives, which are the reason for the maxima. If the process time scale is long in comparison with individual half-lives, a steady-flow equilibrium will be established. When the process time is comparable to or shorter than individual half-lives, a steady flow will not be attained. Thus, the poor agreement beyond the maxima is an indication that the r-process time scale must be comparable to (or at least not much longer than) the longest half-lives, which occur in the path closest to stability at magic neutron numbers. If, on the other hand, the process time is longer than the half-lives in the left wing of the abundance peaks (which is due to nuclei at magic numbers, but with $Z < Z_{\rm peak}$), it will also be longer than the even shorter half-lives for nuclei in between magic numbers. Therefore, it is more reasonable in a steady-flow assumption to fit abundances in between peaks including the left wings, than the whole peaks because the assumption breaks down in the right wings.

Figures 9*a* and 9*b* display the whole region between the $A \simeq 130$ and $A \simeq 195$ peaks for the same n_n-T_9 conditions as in Figure 8, calculated within our unified approach (Möller et al. 1990, 1992a). Again, we see what an improving effect beta-

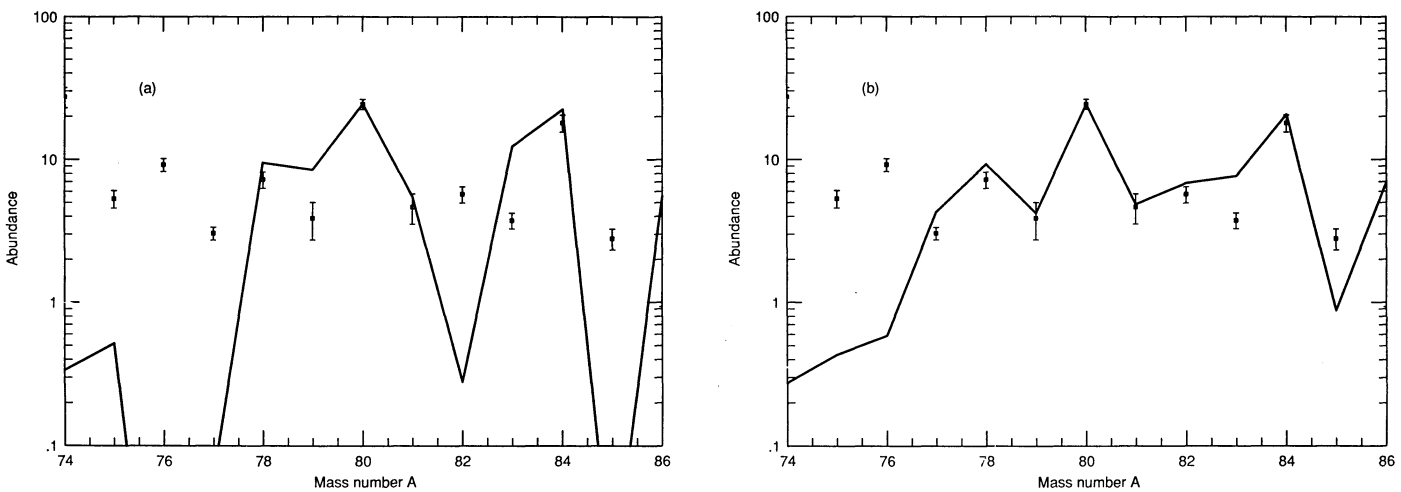

FIG. 7.—Best fit for r-abundances around the $A \simeq 80$ peak with $T_9 = 1.35$ and $n_n = 2.67 \times 10^{20}$ cm^{-3}, normalized to the observed abundance of ^{80}Se: (*a*) progenitor abundances before beta decay; (*b*) final abundances after beta decay and beta-delayed neutron emission. The open squares represent the solar r-process abundances (Käppeler et al. 1989). The odd-even staggering of the solar abundances persists from the original distribution due to (experimentally known) odd-even staggering in the delayed neutron emission probabilities (P_n) of the progenitor isotopes in or close to the r-process path, i.e., ^{79}Cu to ^{85}As. The deviations below $A = 77$ indicate that these isotopes (^{76}Ge, ^{75}As, ^{74}Ge, ...) are not of *classical* r-process origin.

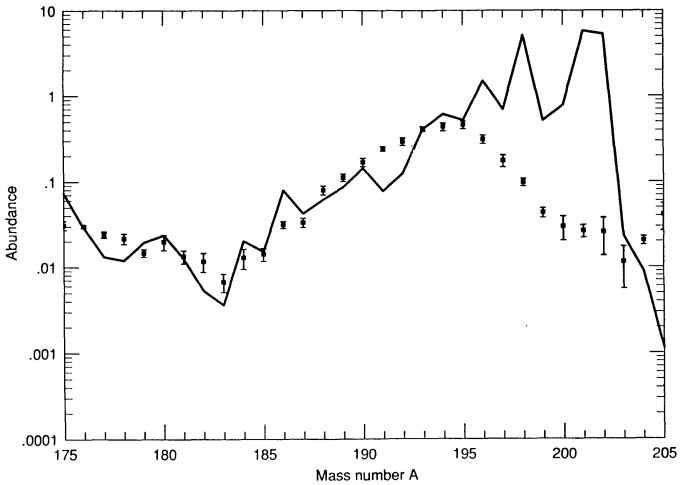

FIG. 8.—Best fit for abundances after beta decay in the $A \simeq 195$ peak region for freeze-out conditions ($T_9 = 1.2$, $n_n = 3.0 \times 10^{22}$ cm^{-3}, normalized to the abundance of ^{193}Ir. The deviations beyond $A = 195$ indicate that above the $N = 126$ closed neutron shell the steady-flow approximation becomes invalid.

delayed neutron emission has on smoothing the abundance curve. In addition, one notices a local deficiency around $A \simeq 142$, the origin of which is due to a local overestimation of the $Z = 50$, $N = 82$ shell strength in the model of Möller et al., as will be discussed later. Apart from this trough, quite decent agreement is found from $A \simeq 145$ through the $A \simeq 195$ peak. The same test can be performed for the region below the $A \simeq 130$ peak. In Figures 10*a* and 10*b* we show the best fit obtained for $n_n = 9.5 \times 10^{20}$ cm^{-3} and $T_9 = 1.2$. Here, the comparison is not between abundances before and after beta decay but between (*a*) using the Möller et al. (1992b) masses and (*b*) substituting for $39 \leq Z \leq 53$ the masses from the Hilf et al. (1976) predictions. The general trend is the same as in Figures 9*a* and 9*b*, but now a big trough occurs *below* the $A \simeq 130$ peak, i.e., in the $115 \leq A \leq 125$ mass region. This deficiency is somewhat improved when using the Hilf mass formula, but still the agreement is not overwhelming.

The reason for the abundance trough around $A \simeq 120$ is clarified in Figures 11*a* and 11*b*. The strong shell corrections of the $N = 82$ shell move the path directly from $(Z, N) = (40, 72)$ to $(Z, N) = (41, 81)$, before, at (42, 82), the magic neutron number is reached, leaving a gap in A of 10 units. The abundance of any nucleus with an intermediate A is very small (only isotopes with more than 10% population of their Z-chain are plotted), so that a huge gap exists in the *r*-process path, which cannot be filled completely by beta-delayed neutron emission. It should also be mentioned here that the same shell-strength arguments can be applied to explain the (smaller) trough around $A \simeq 142$. Surprisingly, the less sophisticated mass model by Hilf et al. (1976) seems to perform slightly better in these regions (Figs. 10*b* and 11*b*), but it is clear that for both mass models this transitional region, from deformed isotopes via spherical nuclei (around $N = 82$) again to deformed isotopes, is problematic (for a more detailed discussion see § 6).

Despite these "quantitative" problems, we can conclude this subsection with the following result: three sets of steady-flow calculations can reproduce the regions $135 \leq A \leq 195$, $90 \leq A \leq 133$, and $77 \leq A \leq 85$. Nuclei below $A = 77$ seem not to originate from *r*-process conditions. The differences of solar abundances and *s*-process contributions for this region must result from a type of neutron-rich freeze-out of explosive Si burning (see, e.g., Hartmann, Woosley, & El Eid 1985 or Thielemann, Hashimoto, & Nomoto 1990) but are not of a genuine *r*-process origin. The areas between the three regions experience a breakdown of the steady-flow assumption, due to long half-lives, which are comparable to or longer than the process time scale. This is similar to the *s*-process, which experiences an approximate steady flow (of neutron captures and thus constant $Y_i \sigma_i$—the product of abundances and neutron-capture cross sections) in between magic neutron numbers, where the cross sections are smallest. Because in the *r*-process the time scales of neutron captures are faster than beta decays (opposite to the *s*-process), the roles of neutron captures and beta-decay rates are exchanged and we find $Y_i \lambda_\beta^i \simeq$ constant, except for the breaks at magic numbers.

The results given in this subsection can be generalized. These best-fit conditions for certain regions are not only found for the

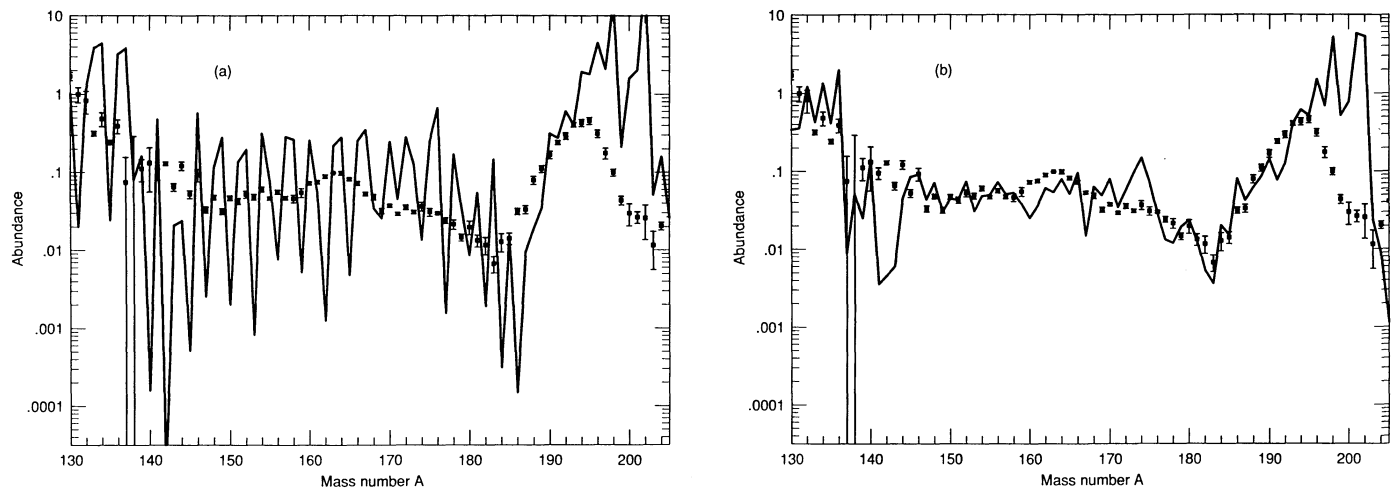

FIG. 9.—Best fit for *r*-abundances in the mass range $135 \leq A \leq 205$ for freeze-out conditions as in Fig. 8: (*a*) progenitor abundances before beta decay; (*b*) final abundances after beta decay and delayed neutron emission. The deviations for $A > 195$ again indicate the breakdown of the steady flow beyond the $N = 126$ neutron shell closure.

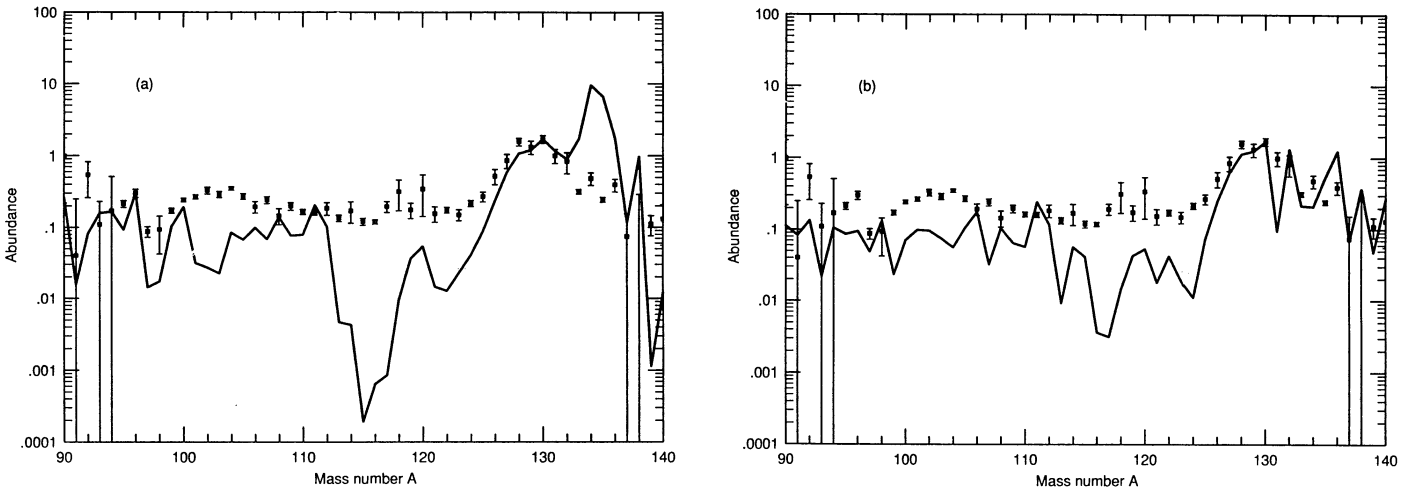

FIG. 10. Best fits for r-abundances, in the mass range $90 \leq A \leq 140$ for freeze-out conditions ($T_9 = 1.2$, $n_n = 9.5 \times 10^{20}$ cm^{-3}), normalized to the observed abundance of ^{130}Te, after beta decay: (*a*) B_n values from the Möller et al. mass model were used to determine the r-process path; (*b*) for $A \geq 110$ the Möller et al. B_n values are replaced by those from the Hilf et al. mass formula. The deviations beyond $A = 130$ indicate that above the $N = 82$ closed neutron shell the steady-flow approximation is no longer valid. The underestimate of the calculated abundances for $A \leq 126$ originates predominantly from deficiencies in the mass model predictions (see text).

n_n-T_9 values given in Figures 7, 9, and 10, but everywhere on the lines in the n_n-T_9 plane as summarized in Figure 12. $A \simeq 80$, $A \simeq 130$, and $A \simeq 195$ stand for the $A \simeq 80$ peak and the regions $A \leq 130$ and $A \leq 195$, respectively. The values used in the present demonstrations are close to the $(n, \gamma) \rightleftharpoons (\gamma, n)$ freeze-out conditions. In an earlier exploratory study, Thielemann et al. (1992) found similar results, but the analysis was performed only for one temperature, $T_9 = 1.3$. They also found two local minima in the abundance fits just for the $A \simeq 195$ peak. We present here only the one which also reproduces the region between $A \simeq 130$ and $A \simeq 195$. Thielemann et al. also tested different combinations of mass-model and half-life sets, obtaining similar but somewhat different n_n-T_9 conditions. Here we focus on our *consistent* set of masses and half-lives discussed in § 3. There remains, however, an uncertainty for the conditions which reproduce nuclei beyond $A \simeq 200$. We indicate one set of conditions with a dashed line in Figure 12. But because of the instability of nuclei for $A > 209$, there is no simple shape to fit, and this study is just exploratory (for more details see § 5.4).

One final question remains, after conditions have been found which nicely reproduce subsets of the solar r-abundances. Can the global r-abundance curve be the result of a superposition of three (or more) *global* steady flows, where each component dominates one peak and therefore simulates a curve which seems to indicate an $(n, \gamma) \rightleftharpoons (\gamma, n)$ and steady-flow equilibrium? This is not possible, as already shown in Figure 6; the curve reproducing the $A \simeq 80$ peak is overproducing the $A \simeq 130$ and $A \simeq 195$ peaks, thus dominating their abundances. The same would be the case for the global curve, fitting the $A \simeq 130$ peak with respect to the $A \simeq 195$ peak. A superposition would only make sense when the abundances for an

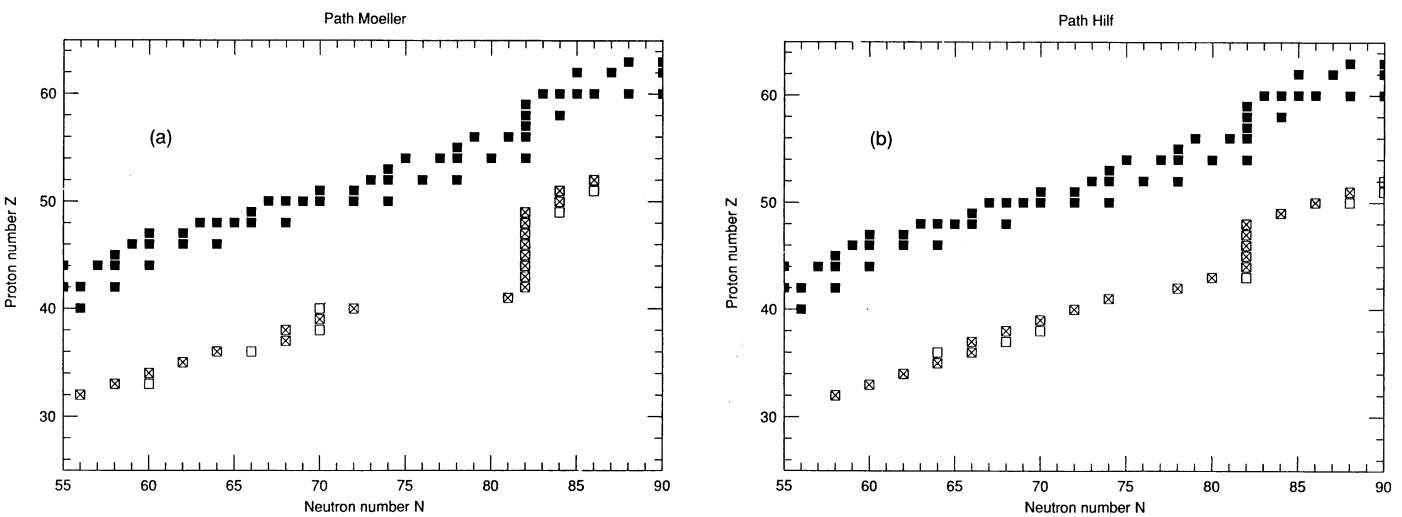

FIG. 11.—Schematic view of the r-process path in the $85 \simeq A \simeq 140$ mass region for freeze-out conditions ($T_9 = 1.2$, $n_n = 9.5 \times 10^{20}$ cm^{-3}) as in Fig. 10, containing nuclei with $B_n \simeq 2$ MeV. Shown are those isotopes with more than 10% population of each isotopic chain: (*a*) When using the mass model of Möller et al., one observes beyond $^{112}_{40}Zr_{72}$ a region of 9–10 masses where obviously no isotope with appropriate B_n value exists. Due to the strong shell strength in this mass model a sudden drop from $B_n \geq 3$ MeV to $B_n < 1$ MeV (see also Fig. 20) occurs close to the magic neutron number. (*b*) The Hilf et al. mass formula has obviously a smoother decrease in B_n values so that several isotopes exist in the r-process path between $A = 112$ and $A = 125$.

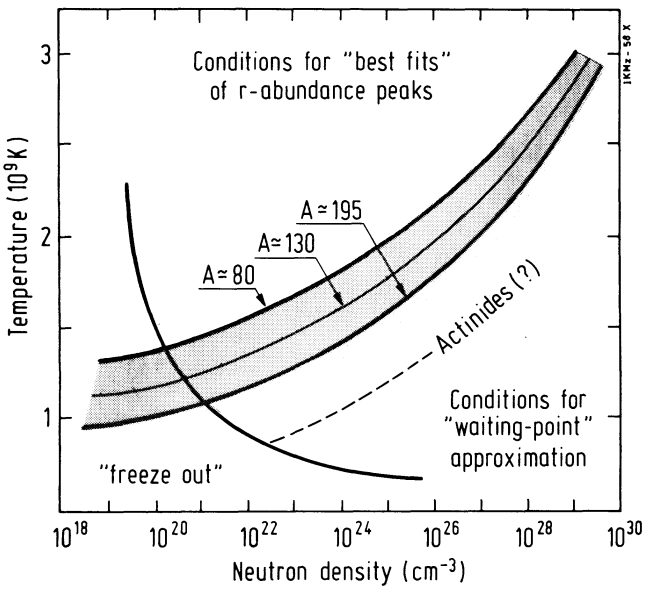

FIG. 12.—Same as Fig. 4, indicating, however, in detail the parts of the n_n-T_9 band which are responsible for different mass ranges of the solar r-process abundance. A superposition of at least three components is required to reproduce the $A \simeq 80$ peak and the two mass ranges $90 \leq A \leq 130$ and $135 \leq A \leq 195$. Because nuclei between Bi and the actinides decay via alpha-decay chains, no clear features emerge for a best fit. The dashed line labeled actinides only indicates a first guess.

n_n-T_9 condition, appropriate to the region around $A \leq A_{peak}$, would be set to zero for $A > A_{peak}$. Such a situation can occur in a time-dependent calculation, where only abundances up to A_{peak} are formed yet. The peaks containing nuclei with the longest half-lives (0.2–0.5 s) act as longest waiting points, over which only small amounts of matter will pass. This corresponds to the picture summarized in Figure 13 for the four different r-process components. Therefore, we will now test

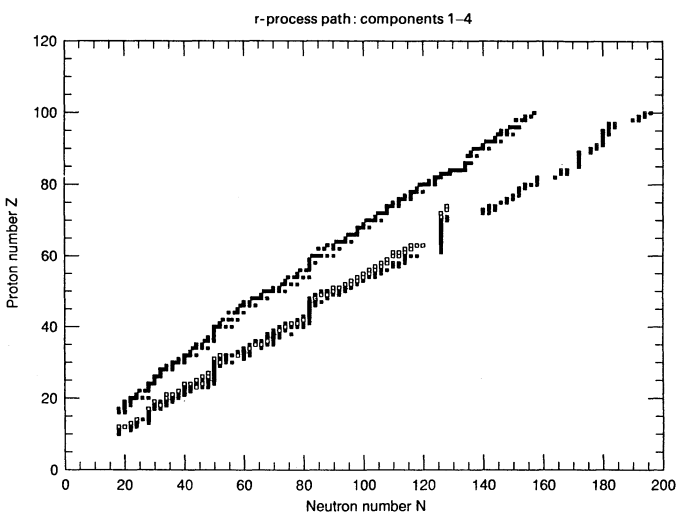

FIG. 13.—The r-process paths of all four components are shown. Open squares are for components 1 and 3 (going slightly beyond $N = 50$ and $N = 126$), solid squares for components 2 and 4 (up to $N = 82$ and beyond $N = 126$). This emphasizes that there is not one unique r-process path which reproduces the whole solar r-abundance curve. But between two magic neutron numbers only one path is responsible for the solar r-abundances in this mass range.

the n_n-T_9 sets, found for local steady flows, in time-dependent calculations.

5.3. *Time-dependent Calculations*

In these calculations, we still make use of an $(n, \gamma) \rightleftharpoons (\gamma, n)$ equilibrium but give up the global steady-flow assumption. Equation (4) provides $Y(Z)$ as a function of time t. The initial conditions are defined by $Y(Z_{min}, t = 0)$ and $Y(Z > Z_{min}, t = 0) = 0$. We chose to start our calculations with $Z = 26$. When using the three selected n_n-T_9 sets for the individual peaks which gave the best fits in a local steady-flow approach (see § 5.2), one obtains three different r-process paths, with the top of the $A \simeq 80$ peak being reached for $Z = 30$, the $A \simeq 130$ peak maximum for $Z = 48$, and the $A \simeq 195$ peak for $Z = 69$. The time scales for reaching the appropriate peaks are comparable. They are of the order of 1.5–2.5 s, which is consistent with the expected duration of the r-process in a supernova (a few seconds). Most of the time is spent in the kinks of the r-process paths (Fig. 13) at magic neutron numbers (e.g., for the n_n-T_9 conditions of the $A \simeq 130$ line of Figure 12, 1.5 s are necessary to move from $Z = 26$ to $Z = 44$, whereas 3.5 s would be necessary to move from $Z = 44$ to $Z = 51$). The nuclei beyond the top of each kink with the longest half-lives (e.g., $^{131}_{49}$In and $^{134}_{50}$Sn in the case of the $A \simeq 130$ peak) form the strongest bottlenecks in the r-process flow.

Figures 14*a*–14*d* show four snapshots of that time-dependent evolution where one can witness how matter passes through all peaks as a function of time. One also sees that this n_n-T_9 set would reproduce an $A \simeq 80$ peak at too small an A and an $A \simeq 195$ peak at $A > 195$, in accordance with the discussions in §§ 5.1 and 5.2. Typical r-process half-lives in between magic numbers are of the order of 0.01–0.02 s. In the peak, half-lives are of the order of 0.2–0.5 s. Within 1.7 s, the bulk of the matter reaches the $A \simeq 130$ peak, while the plateau for $A < 130$ is still filled, and a fit similar to the steady-flow calculations for the same n_n-T_9 conditions of § 5.2 is obtained. Figure 15 shows the product $Y(Z)\lambda_\beta(Z)$ of equation (5), and we see that the near-constancy for the range $86 \leq A \leq 130$ at $t = 1.7$ s validates the steady-flow approach taken in § 5.2. In the case of a calculation which keeps the seed nucleus constant [$Y(Z = 26, t) = \text{constant} = Y(Z = 26, 0)$], a steady flow would always occur after a sufficient time period, larger than the sum of all half-lives in the r-process path. When starting with a specific $Y(Z_{min}, 0)$, which can be depleted afterward, the leakage toward heavier nuclei will make a steady-flow assumption invalid after a given time. At $t = 1.7$ s, however, when also the best fit results, a steady flow is valid in the range $86 \leq A \leq 130$.

Figure 16 shows the results of similar time-dependent calculations which reproduce the $A \simeq 80$ peak and the $135 \leq A \leq 195$ region at 1.5 and 2.5 s, respectively. A choice of $Z_{min} = 40$ rather than 26 (a heavier seed nucleus) for the third component would give the same result in 1.5 s rather than 2.5 s. When either several astrophysical events or different zones with varying conditions in one event create these abundance patterns, a superposition—weighing the different components appropriately—can reproduce the *global* r-abundance curve. This is shown in Figure 17. The statistical weights of the three components are 10:2.6:1. A discussion about these weights and the apparently slightly different time scales for the three components will be part of § 7. A realistic model will certainly be a superposition of more than the three zones which, with the appropriate weight factors, might yield further improvements.

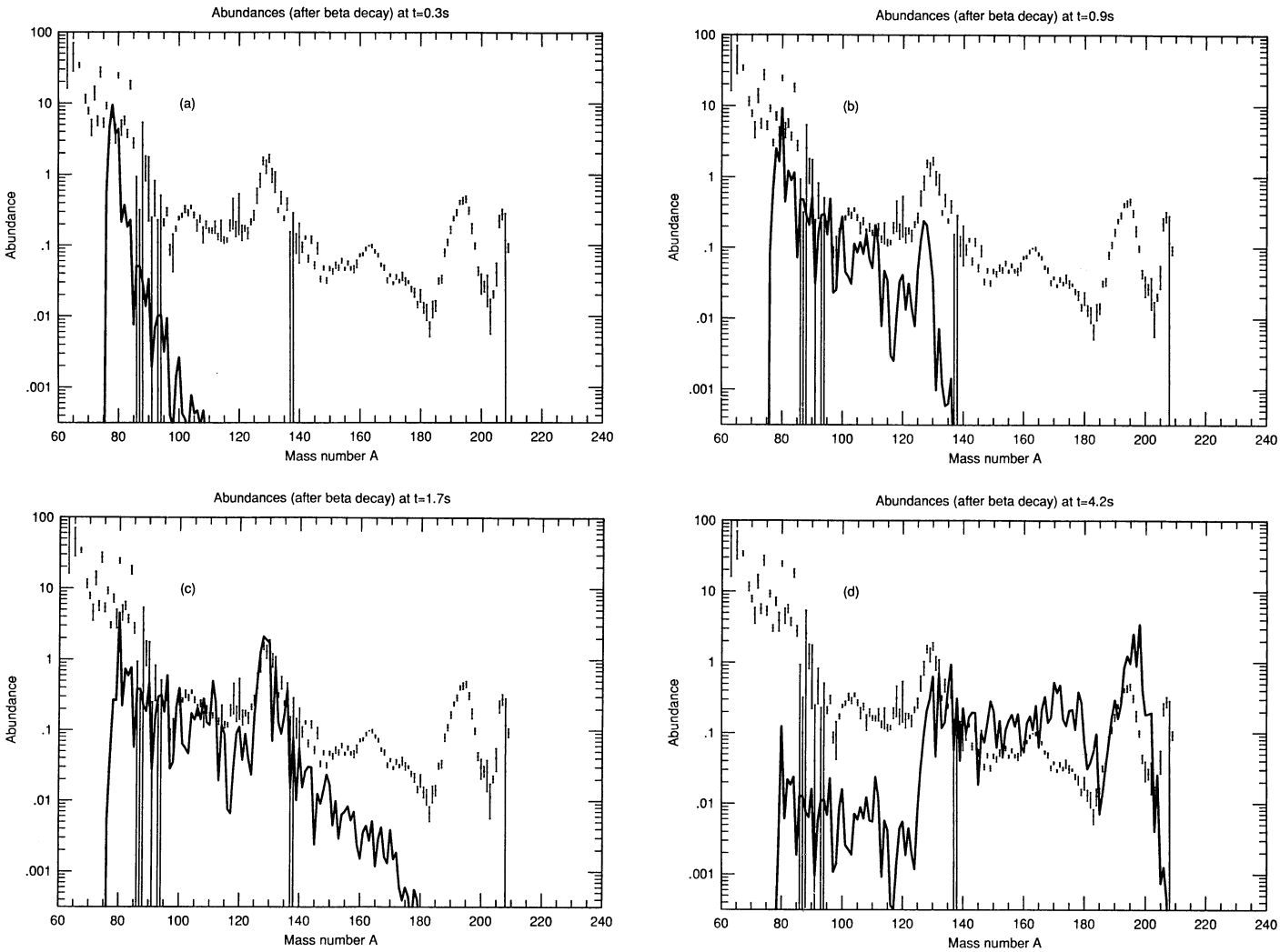

FIG. 14.—Time-dependent calculation with best-fit conditions for the mass range $90 \leq A \leq 130$ (see Fig. 10). Panels *a–d* display a time sequence. Times (after beta decay): (*a*) $t = 0.3$ s; (*b*) $t = 0.9$ s; (*c*) $t = 1.7$ s; (*d*) $t = 4.2$ s. After 1.7 s, starting from an initial seed nucleus with $Z = 26$, an almost identical result to the best fit of Fig. 10 is obtained. During the time evolution the peaks at $A \simeq 80$ and $A \simeq 195$ are also produced. However, the conditions which fit best the mass range $90 \leq A \leq 130$ yield the $A \simeq 80$ peak at too low mass numbers and the $A \simeq 195$ peak at too large mass numbers.

At this point, let us note that the overall agreement of the global abundance curve looks quite impressive; clearly, the main features are reproduced. However, there remain several deficiencies, as indicated in the lower part of the curve. At small A-values we notice that there exists no good fit for nuclei with $A = 77$–79, whereas we could fit them in a steady-flow calculation. This can be changed by a shorter duration time or by starting with a lower Z for the seed nuclei. Then, one can obtain the $A \simeq 80$ peak down to $A = 77$. Specifically, large discrepancies like the trough at $115 \leq A \leq 125$ and the spikes at $A \simeq 111$ and $A \simeq 175$ will not vanish with such adjustments. They must have a different explanation. The origin of the trough in the region $115 \leq A \leq 125$ has already been discussed in § 5.2. An explanation of this and other deviations from the solar r-abundance curve via nuclear properties will be given in § 6. Although, partly because of the above deficiencies, the agreement between calculated and observed r-abundances is not yet perfect, it has reached a point where the abundance curve can outline individual problems in the prediction of nuclear data. Thus, in general, one can claim now that *isotopic abundances* become meaningful.

5.4. *Actinides and Chronometers*

With the set of n_n-T_9 values indicated by the three solid lines in Figure 12, we obtain only nuclei up to $A \simeq 200$. There is, however, no reason not to add an additional component with a larger n_n that would produce heavier nuclei. For example, Figure 18 gives the result for a superposition of four components where the last one has a neutron density as high as 10^{27} cm^{-3}. This component has to reproduce all nuclei beyond $A = 203$, i.e., ^{203}Tl, ^{204}Hg, ^{205}Tl, ^{206,207,208}Pb, and ^{209}Bi. In addition, the long-lived r-process chronometers ^{232}Th, ^{238}U, and ^{235}U are also produced by this component. Using production ratios of these chronometers, together with the isotopic abundances at the time of the formation of the solar system (from meteoritic abundances) and knowledge about the history of star formation in the Galaxy, Galactic age determinations can be made (for more general recent reviews, includ-

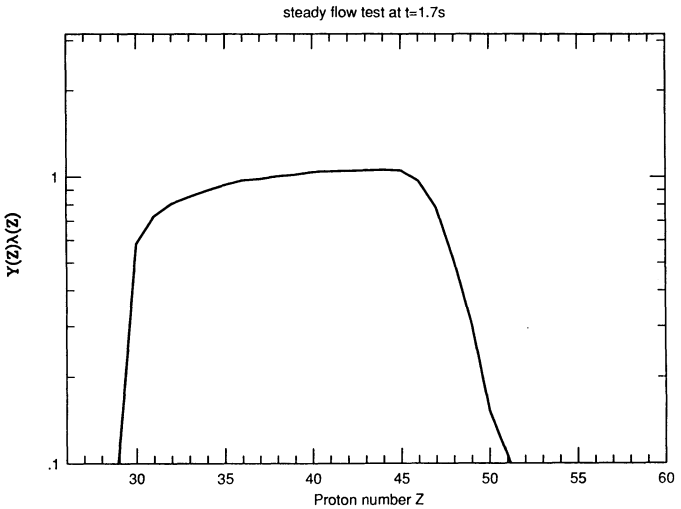

FIG. 15.—Plot of $Y(Z)\lambda_\beta(Z)$ as a function of charge number Z at $t = 1.7$ s, which coincides with the abundance pattern of Fig. 14*c*. The ordinate is shown in arbitrary units. The near-constancy of the curve for the Z-range responsible for abundances in the mass range $90 \leq A \leq 130$ is a proof of the steady flow in this time-dependent calculation and validates the analysis of § 5.2.

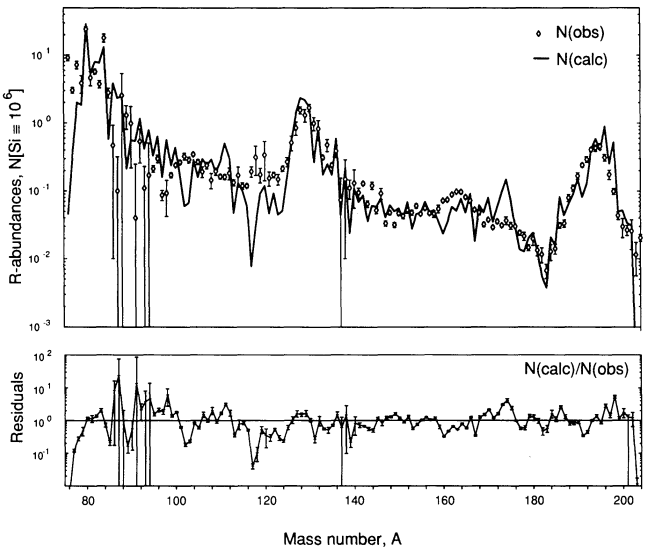

FIG. 17.—Global r-abundance curve obtained from a superposition of three time-dependent calculations with the best-fit n_n-T_9 values for the $A \simeq 80$ peak and the $90 \leq A \leq 130$ and $135 \leq A \leq 195$ mass ranges. The weight of the individual components is 10:2.6:1. In the lower part the ratios of calculated and observed r-abundances are shown. The discussion of the largest deviations at $A = 112$, 115–125, and 176 will be part of § 6.

ing a description of galactic evolution models, see Cowan, Thielemann, & Truran 1991a, b).

In the r-process, the final abundances of these long-lived isotopes involve summations over the abundances of a number of short-lived progenitors in alpha-decay chains, such as ^{232}Th, ^{236}U, ^{240}Pu, ^{244}Pu, ^{248}Cm, and ^{252}Cf; ^{235}U, ^{239}Pu, ^{243}Am, ^{247}Cm, ^{251}Cf, and ^{255}Fm; ^{238}U, ^{242}Pu, ^{246}Cm, and ^{250}Cf; and ^{244}Pu, ^{248}Cm, and ^{252}Cf, to predict the production ratios of the actinide pairs ^{232}Th/^{238}U, ^{235}U/^{238}U, and ^{244}Pu/^{238}U. The isotopes ^{206,207,208}Pb and ^{209}Bi have, in addition to the direct beta decay from the r-process path, also such an indirect component from alpha-decay chains of unstable nuclei beyond $A = 209$. In each of these summations, the number of progenitors is constrained by a line, beyond which spontaneous fission dominates all other modes of decay.

The fact that there is not an extended abundance pattern of such stable nuclei which can be fitted makes the n_n-T fit of this component harder. Additional complications come from the long-lived actinides which change the population of the Pb and Bi isotopes in a time-dependent way. Finally, it is not clear whether a third (the strong) s-process component (Beer & Macklin 1985; Käppeler et al. 1989) contributes significantly to these isotopes, thus making it even unclear what r-process component is really required and should be fitted. For these reasons we did not make the attempt in this paper to determine the best-fit conditions for this mass region. When it will be done, such an analysis will also be affected by possible uncertainties in masses (Wu et al. 1987; Han et al. 1992; Wang et al.

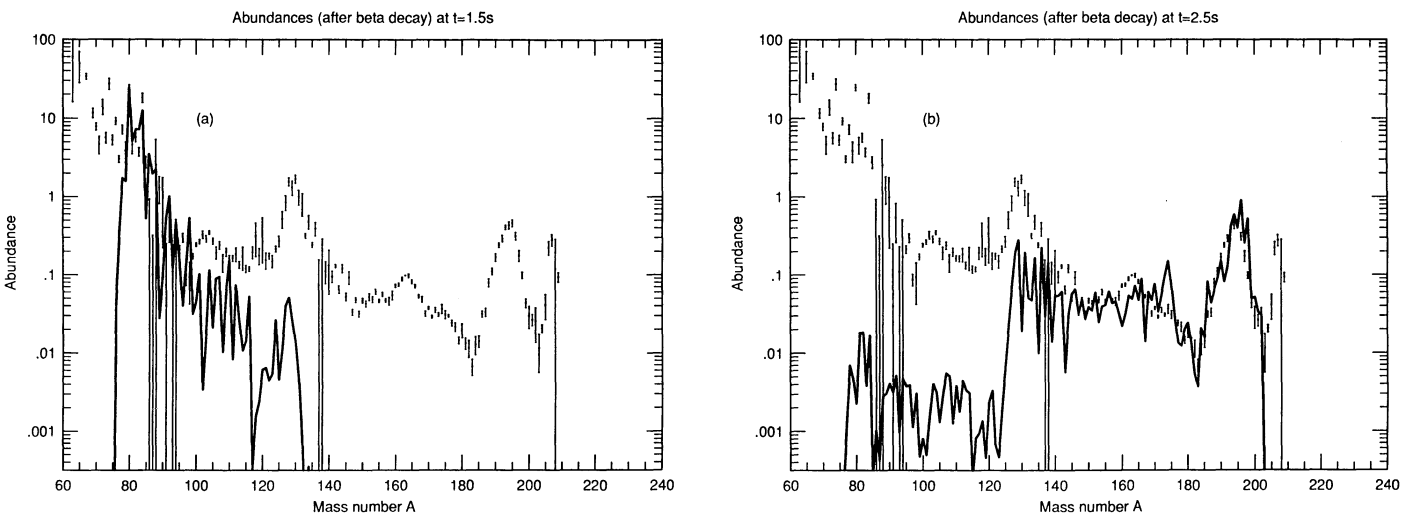

FIG. 16.—Same as Fig. 14: (*a*) The conditions of Fig. 7 lead to the formation of nuclei in the $A \simeq 80$ peak at $t = 1.5$ s (after beta decay) for a seed nucleus with $Z = 26$. This duration is sufficient to build up the $A \simeq 80$ peak, but declines steeply for larger mass numbers. (*b*) The conditions of Fig. 9 lead to the formation of nuclei beyond $A \simeq 130$ up to the $A \simeq 195$ abundance peak after $t = 2.5$ s (after beta decay). If a seed nucleus with $Z = 40$ is chosen, the same configuration occurs at $t = 1.5$ s.

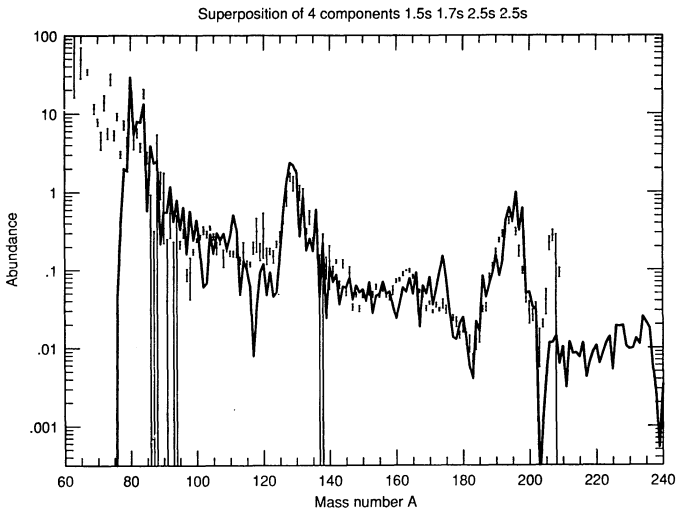

FIG. 18.—Same as Fig. 17, but with an additional component superposed which leads to an *r*-process path far enough from stability so that during 1.5 s even nuclei beyond the $A \simeq 195$ peak are produced. Stable Pb and Bi isotopes will get (large) contributions from alpha-decay chains. Times are $t = 1.5$ s, 1.7 s, 2.5 s, and 2.5 s.

1992) and a new evaluation of fission properties (Meyer et al. 1989).

6. LEARNING NUCLEAR STRUCTURE FROM *r*-PROCESS ABUNDANCES?

As we have seen from Figures 17 and 18, by superposing three or four *r*-process components with different neutron number densities (see Fig. 12) we can obtain quite good overall agreement between observed and calculated *r*-process abundances. However, when taking a closer look at the abundance distribution, several distinct deviations can be recognized (most clearly seen in the "residuals" N(calc)/N(obs) in the lower part of Fig. 17), which may be signatures of structure effects not contained or not accounted for properly in our *unified*, but still too simplistic approach of calculating nuclear physics parameters (see § 3). In the following we will try to identify the possible origin of these abundance deviations.

Apart from the region below $A \simeq 80$, where the underestimation of the *r*-abundances is due to *astro*physical reasons [the *r*-process residuals $N(\text{obs}) \simeq N_\odot - N_s$ are not of genuine *r*-origin], and the $A \simeq 90$ region, where the N(obs) have very large uncertainties, there are three mass ranges of particular interest. These are the region around $A \simeq 120$ already mentioned in § 5 and the mass ranges $100 \leq A \leq 115$ and $160 \leq A \leq 180$, where sinusoidal deviations show up. Since, with slight variations in magnitude and position, these local under- or overestimations of isotopic *r*-abundances are seen in the static equilibrium fits (see Figs. 6*a*, 9*b*, and 10*a* and *b*) as well as in the time-dependent calculations (see Figs. 14 and 16), they should—at least to a major extent—reflect nuclear structures very far from beta stability, and *not* deficiencies in the astrophysical parameters T_9, n_n and *r*-process time scale.

6.1. *The $A \simeq 120$ r-Abundance Region*

As already mentioned in § 2, within our steady-flow approach the *r*-abundances are mainly determined by the $T_{1/2}$ (and P_n branchings) and the neutron-separation energies (B_n) of the waiting-point nuclei. As a result of our best fits for the $90 \leq A \leq 130$ region (Figs. 10*a* and 10*b*), the *r*-process path should mainly run through isotopes with constant $B_n \simeq 2$ MeV. Let us now check the model predictions of all (interrelated) nuclear physics input parameters by using (1) our *unified* approach (see § 3, and see Möller et al. 1990, 1992a) and (2), for comparison in specific mass regions, the predictions from the admittedly less sophisticated model of Hilf et al. (1976). According to both mass models, the *r*-process isotopes in the region between the $A \simeq 80$ and $A \simeq 130$ abundance peaks have Q_β values between 8 and 15 MeV, with the beta-decay energies from the Möller-Nix model being systematically higher by about 500 keV. As a consequence, the calculated beta-decay half-lives for these waiting-point nuclei should be similar, although apart from small Q_β effects also the model-dependent, different deformation parameters (which may lead to substantially different shapes of the calculated GT strength functions; see § 3) may be reflected in the theoretical $T_{1/2}$. And, indeed, for the possible waiting-point candidates in this local region both our calulated $T_{1/2}$ sets agree within a factor of 2, as can be seen from Figure 19. In this context, it may be interesting to compare our $T_{1/2}$ calculations performed with the Hilf et al. Q_β values and deformation parameters (converted from β_2 to ϵ_2) with those by Staudt et al. (1990), who used—including the Nilsson single-particle and BCS pairing models—exactly the same parameter set. The differences to our $T_{1/2}$ [shown as the ratios $T_{1/2}(\bigcirc)/T_{1/2}(\bullet)$ in Fig. 19] are created by an adjustment of the χ_{GT} parameter for each Z to experimentally known half-lives; there is no direct physical understanding of this (especially of why there should be a Z-dependence and no N-dependence). The differences are on the average larger than the ratios $T_{1/2}(\triangle)/T_{1/2}(\bullet)$ from our two QRPA calculations, which contain the combined effects from different Q_β's, deformation parameters, and single-particle and pairing models.

Returning to our discussion of calculated *r*-abundances in the $A \simeq 120$ region, one may, therefore, conclude that the observed large deficiencies cannot be attributed to the theoretical half-lives. In order to reproduce the solar isotopic abundances within our unified approach by *tampering* with the beta-decay half-lives, one would have to assume $T_{1/2}$ of order 1–20 s for isotopes such as ^{115}Nb or ^{116,120}Mo, which is completely unrealistic. Hence, the solution to the problem of the $A \simeq 120$ deficiency must lie in the neutron-separation energies. In Figure 20 we show the B_n values for the potential waiting-point isotopes in the mass regions $107 \leq A \leq 126$ and $133 \leq A \leq 151$, deduced from the mass model of Möller et al. (1992b), in comparison with the values from the Hilf et al. (1976) formula. We notice that between ^{114}Mo and the $N = 82$ isotones the B_n values from the Möller-Nix model lie systematically above those from the older Hilf approach, with a rather abrupt B_n "spike" for those isotopes (^{123}Tc and ^{124}Ru) with one neutron pair less than the magic number $N = 82$. Beyond the $N = 82$ shell, the opposite behavior is observed; up to $N = 90$ (^{142}Te) the Möller-Nix B_n values are lower than those deduced from the Hilf masses. In terms of the "occupation" of an *r*-process path at $B_n \simeq 2$ MeV in the $A \simeq 120$ region, this implies that with the Möller-Nix B_n values, in an extreme view, there would exist *not a single* waiting-point isotope between $^{112}Zr_{72}$ and $^{125}Tc_{82}$ for our best-fit n_n-T_9 conditions (see Figs. 10*a* and 11*a*). Obviously, in the Möller-Nix model the decrease of the neutron-separation energies occurs too slowly when approaching $N = 82$, finally resulting in a sudden drop from $B_n \simeq 3$ to ≤ 1 MeV for the magic neutron number waiting-point nuclei. As has already

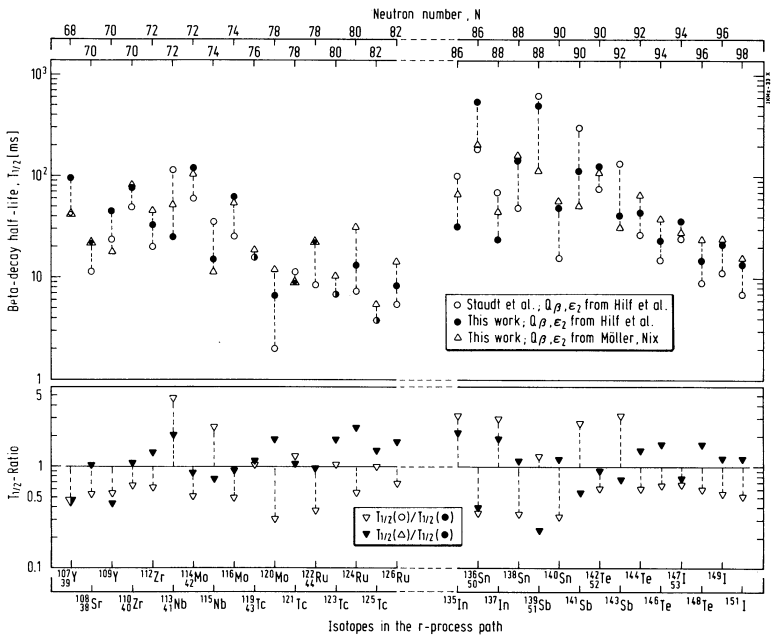

FIG. 19.—Half-life predictions of nuclei in the *r*-process path for the mass range $A = 107$–151 (see Fig. 13) from three different QRPA calculations. *Triangles*: unified model discussed in § 3; *filled circles*: making use of the beta-decay Q-values and deformations by the Hilf et al. mass formula; *open circles*: from Staudt et al. with the Hilf et al. masses.

been discussed in § 3, this model "deficiency" may have its origin in the neglect of the proton-neutron residual interaction which seems to manifest itself in an overestimation of the $Z = 50$ and $N = 82$ shell strengths below $^{132}_{50}Sn_{82}$. This seems to affect the $Z > 40$, $A \simeq 120$ region very far from stability. Presumably, this causes the behavior of the neutron-separation energies and the large *r*-abundance trough when applying the Möller-Nix mass model. When using, instead, the B_n values from the more simplistic Hilf et al. model (which also neglects proton-neutron interactions, but by construction and maybe intuition gives a more smoothly decreasing B_n trend toward $N = 82$; see Fig. 20), at least two more isotopes, ^{115}Nb and ^{120}Mo, will lie in the $B_n \simeq 2$ MeV *r*-process path, which leads to a partial filling of the $A \simeq 120$ *r*-abundance trough (see Figs. 10 and 11). However, even with this additional contribution, our calculated *r*-abundances are still too low in this mass region, on the average by a factor of 5.

One could consider possible astrophysical reasons, e.g., contributions from a "fast *s*-process" (Cameron, Thielemann, & Cowan 1992), which would question the *s*-process/*r*-process

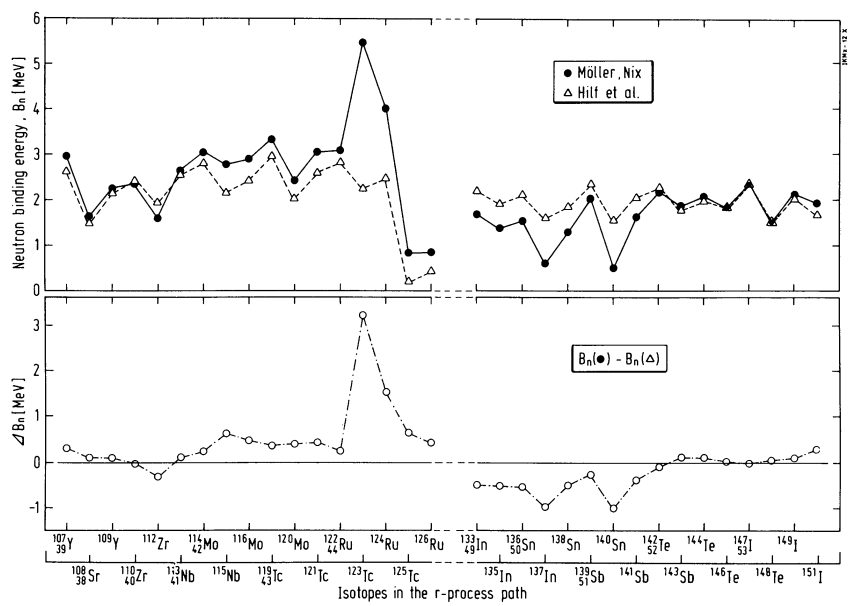

FIG. 20.—Neutron separation (or binding) energies for nuclei around the $A \simeq 130$ peak. Before the shell closure at $N = 82$ the Möller et al. masses give larger B_n values and would thus predict a path farther from stability than the Hilf et al. masses. Thus shorter half-lives are encountered and smaller *r*-process abundances predicted. Beyond the $N = 82$ shell closure the roles and results of both mass models are reversed.

decomposition in this mass region. In pulsed *s*-process calculations (e.g., Hollowell & Iben 1989; Gallino et al. 1990) a first high neutron flux pulse (10^8–10^9 cm^{-3}), due to $^{13}C(\alpha, n)^{16}O$, also produces isotopes which ordinarily result from an *r*-process. However, present calculations (Beer 1991; Käppeler et al. 1991) predict that in the second low flux pulse, due to $^{22}Ne(\alpha, n)^{25}Mg$, these isotopes undergo further neutron captures and the fingerprint of a typical *s*-process pattern is left. In such a case only minor amounts of these isotopes might survive and could be only detectable as extinct radioactivities in the solar system (when the last *r*-process event, producing the majority of these isotopes, occurred long before the last *s*-process contribution and its unstable species decayed in the meantime). This means that these isotopes are not a major component of the *s*-process, and the *r*-process component in the compilation of Käppeler et al. (1989) is not misrepresented.

When there are no astrophysical reasons why the solar *r*-process abundances are incorrect in this mass region, a nuclear explanation has to be found. One may then wonder whether the calculated *r*-abundance "hole" in the $A \simeq 120$ region reflects only the shell strength persisting below $^{132}_{50}Sn_{82}$ or also another effect like unexpectedly "long" beta-decay half-lives. And, indeed, this seems not impossible, provided that the respective waiting-point isotopes exhibit some kind of shape coexistence. This phenomenon has been observed in transitional regions, e.g., around $A \simeq 65$ in Fe-Co-Ni isotopes below the doubly magic ^{78}Ni, in the $N = 58$ and $N = 59$ isotones of Sr–Zr, and also in the $A \simeq 110$ Tc–Ru region. As was discussed in § 3, because of the model-inherent assumption of equal deformation for mother and daughter nucleus in our QRPA calculations (Möller & Randrup 1990), we cannot properly treat beta decays to isotopes with shape coexistence, which would require taking into account partial hindrance of specific GT transitions. In such cases, our model (almost) always calculates too short half-lives. To give a few representative examples, for the ^{97}Rb decay we underestimate $T_{1/2}$ by a factor of 3, for ^{63,67}Co it is a factor of 5, and, as an extreme case, for ^{63}Fe (see, e.g., Möller et al. 1990) our theoretical $T_{1/2}$ is too short by a factor of 30 (!). Based on our present understanding of nuclear structure very far from stability on both sides of the $A \simeq 120$ region (i.e., the development of collectivity in the $50 \leq N \leq 65$, $85 \leq A \leq 105$ mass range (see, e.g., Eberth et al. 1988 and references therein), and the observation of the weakening of the shell strength as well as the dramatic lowering of the $vg_{7/2}$ orbit around $^{132}_{50}Sn_{82}$ (see, e.g., Heyde, Sau, & Meldeghem 1981; Blomqvist 1981), it is quite possible that the phenomenon of shape coexistence may also occur in a small region around $A \simeq 120$ for our waiting-point isotopes. Possible candidates could be ^{120}Mo, ^{119,121,123}Tc, and ^{122,124}Ru (see Figs. 19 and 20).

6.2. *The* $100 \simeq A \simeq 115$ *Region*

As can be seen from Figure 21, obviously correlated with the too slow decrease of B_n, the Möller-Nix model predicts ground-state deformation (with an abrupt change from prolate to oblate shapes for $42 \leq Z \leq 46$ around $N \simeq 72$) up to $N = 80$. In contrast, the older Hilf mass model obtains a smoother decrease of (by construction exclusively *prolate*) deformation as a consequence of the assumption of "symmetry" relative to the $N = 66$ neutron mid-shell, reaching spherical ground-state shapes already around $N = 78$. Remembering that the Möller-Nix mass model predicts the onset of deformation in the neutron-rich $A \simeq 100$ region too early (see discussion in § 3), one may suspect that—although using a microscopic single-particle model—deformed shapes will also be maintained too long. The same conclusion would also arise from a quite different, empirical but successful approach of "counting" the number of valence-nucleon (*nn* and *pp*) pairs or (*nn-pp*) quartets (see, e.g., Casten 1985a, b; Pfeiffer & Kratz 1987) in this mass region. This phenomenological model defines $^{98}_{38}Sr_{60}$ as the (unique) candidate for optimum neutron-to-proton composition in terms of valence *nn-pp* quartets, exhibiting maximum possible ground-state deformation in the $A \simeq 100$ mass region. And this has, indeed, been observed experimentally (Ohm et al. 1987; Lhersonneau et al. 1990, 1991). Within the above model, adding further proton (or neutron) pairs beyond $Z = 38$ (resp. $N = 66$) will not lead to another increase of deformation but rather to a (smooth) decrease. Since the underlying proton-neutron interactions, which are assumed to generate these effects, are not contained in the Möller et al. mass and QRPA models, the predicted ground-state deformations in the $Z \leq 38$, $N \leq 66$ region (see Fig. 21) may well be too high. And we believe that this could be the nuclear physics origin of the sinusoidal deviations seen in the $100 \leq A \leq 115$ mass region in both our static equilibrium (Fig. 10) and time-dependent (Figs. 14*c*, 17) *r*-abundance calculations.

The assumption of somewhat lower ground-state deformation for the $N \geq 66$ waiting-point isotopes would require slightly lower B_n values (since these quantities are interrelated in a macroscopic-microscopic mass model). For given n_n-T_9 conditions, this would shift the *r*-process path closer to beta stability, and, in consequence, also change the isotopic *r*-abundance ratios, giving the lighter isotopes a higher weight (see eq. [3]). In our specific case, this would cause a shift of the maximum abundances in the isotopic chains from $^{105}Rb_{68}$, $^{106}Sr_{68}$, $^{109}Y_{70}$, and $^{112}Zr_{72}$ (see Fig. 20) toward their respective $(N - 2)$ isotopes. This results at the same time in a filling of the local $A \simeq 103$ deficiency and in a lowering of the $A \simeq 111$ "spike." An additional modulation of the isotopic abundances will come from changes in the beta-decay half-lives: (1) on the one hand, the $T_{1/2}$ of the $(N - 2)$ isotopes are longer than those of the "original" waiting-point nuclei listed above, again filling the $A \simeq 103$ part of the sinusoidal deviation; (2) on the other hand, with increasing neutron number beyond mid-shell, the theoretical $T_{1/2}$ in the $A \simeq 110$ region will become shorter with decreasing deformation. When viewing, for our best-fit n_n-T_9 conditions, the predicted nuclear properties of the progenitor isotope(s) of the $A \simeq 111$ *r*-abundance "spike," we can trace this back to the $T_{1/2}$ and P_n value of *one single* isotope, i.e., $^{112}Zr_{72}$. As can be seen from Figure 22, assuming—in the spirit of the discussion above—a lower deformation, say $\epsilon_2 \simeq 0.2$, for ^{112}Zr (lying six neutrons beyond mid-shell), leads to a shorter $T_{1/2}$ and a smaller P_n value. According to equation (5), this would result directly in a smaller *r*-abundance of its stable isobar and, as discussed above, would contribute to lowering the $A \simeq 111$ "spike" in our present calculations.

6.3. *The* $160 \simeq A \simeq 180$ *Region*

A similar situation seems to exist in the $160 \leq A \leq 175$ mass region, where the other sinusoidal deviation in the *r*-abundances shows up (see Fig. 9 for our static calculations, and Figs. 16 and 17 for the time-dependent calculations). As can be seen from Figure 21, beyond $N = 82$ the Möller-Nix mass model predicts the onset of deformation for our waiting-point isotopes around $N = 90$. The maximum value of $\epsilon_2 \simeq 0.25$ is

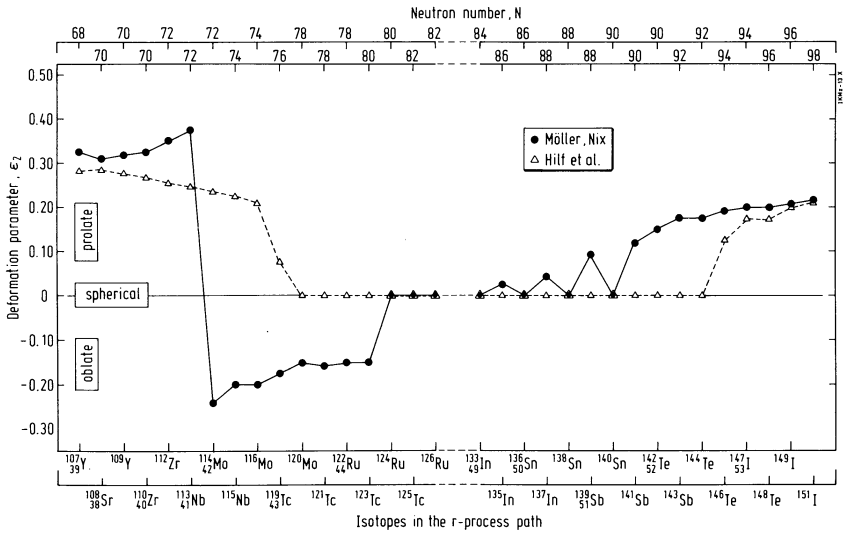

FIG. 21.—Deformation parameter ϵ_2 from the Möller et al. and Hilf et al. mass predictions. We see deviations in the transition behavior from deformed mid-shell nuclei to spherical nuclei at the shell closure.

reached above $A \simeq 150$ and stays practically constant up to the r-process nuclei ^{173,175}Pm. Here deformation starts to decrease slightly up to $A \simeq 180$, where, after a sharp switch from prolate to oblate shape (around $^{183}Eu_{120}$), the r-process path continues with spherical $N = 126$ waiting-point isotopes. In comparison, the Hilf et al. mass formula assumes a somewhat later onset of deformation beyond $N = 82$ (i.e., for the $N = 94$ isotones ^{146}Te and ^{147}I) and reaches the same maximum ϵ_2 values as the Möller-Nix model in the mass region $150 \leq A \leq 165$. After a slight decrease of deformation up to waiting-point isotopes around $N \simeq 114$, $A \simeq 175$, the Hilf model predicts spherical shapes already for nuclei such as $^{178}Sm_{116}$ and $^{179}Eu_{116}$, 10 neutrons below the $N = 126$ magic shell.

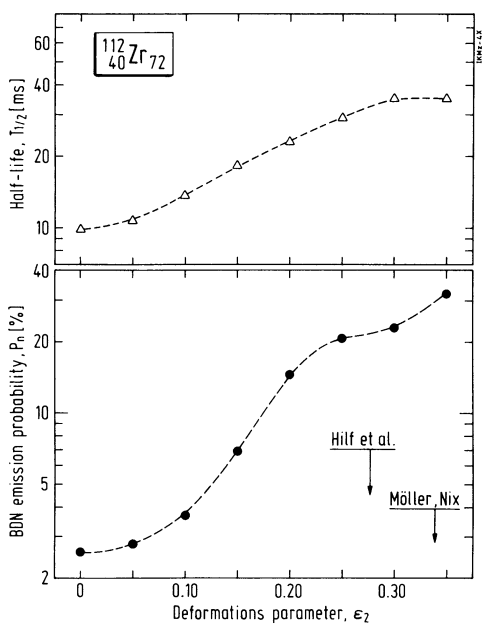

FIG. 22.—Half-life and P_n value predictions for ^{112}Zr as a function of deformation parameter ϵ_2. A smaller deformation than predicted by Möller et al. leads to a reduction of the half-life and thus to a smaller abundance in the r-process path.

As for the $100 \leq A \leq 115$ region, the sinusoidal deviation in the $160 \leq A \leq 180$ mass range probably reflects the interplay between the correlated nuclear properties B_n, ϵ_2, $T_{1/2}$, and P_n and the resulting isotopic r-abundances. For the main waiting-point nuclei beyond the $N = 104$ neutron mid-shell (for our best-fit n_n-T_9 conditions, i.e., ^{163}La, ^{164,166}Ce, ^{167}Pr, ^{170,172}Nd, etc.), the empirical valence-nucleon approach (Casten 1985a, b; Daley et al. 1986) would again suggest a slight decrease of quadrupole deformation. When somewhat lower B_n values are assumed (correlated with smaller deformation), the r-process path would be defined to lie (locally) a little bit closer to beta stability. Again, the combined effects of a shift of the maximum abundances in each isotopic chain from the above waiting-point nuclei toward their $(N - 2)$ isotopes, together with their (on average a factor of 1.4) longer half-lives, would simultaneously result in filling up the $A \simeq 160$ part of the deviation and lowering the $A \simeq 175$ "spike." A closer look at the predicted beta-decay properties for the r-process progenitor(s) of this local deficiency indicates that, as in the case of the $A \simeq 111$ "spike," *one single* isotope, i.e., $^{176}_{62}Sm_{114}$, is responsible (at least for our specific n_n-T_9 conditions; see Figs. 9 and 17) for the $A \simeq 175$ deviation. In Figure 23 we show that a lower deformation for the isotope ^{176}Sm (lying 10 neutrons beyond the $N = 104$ mid-shell) would result in a shorter $T_{1/2}$ and a lower P_n value, thus adding another contribution to smooth out the sinusoidal shape of our calculated r-abundances in this mass region.

There is another interesting observation in the $A \simeq 180$ mass range (see Figs. 8, 16, and 17); here the shape of the *observed* abundance curve resembles to some extent that of the *calculated* distribution in the $A \simeq 120$ region. The fair reproduction of the solar r-abundance trough around $A \simeq 180$ when using the Möller et al. (1990, 1992a) unified approach may indicate the vanishing of the $^{208}_{82}Pb_{126}$ shell strengths only very far from stability—in the vicinity of the $N = 126$ shell, but more than 10 Z-units below the proton-shell closure. It may be interesting to mention in this context that the Hilf mass formula fails to reproduce the observed r-abundance features in both tails of the $A \simeq 195$ peak. Some indication for the $A \simeq 180$ part can be seen from Figures 6*b* and 6*c*. The above result, in turn, may imply for the $A \simeq 120$ mass region that probably also there

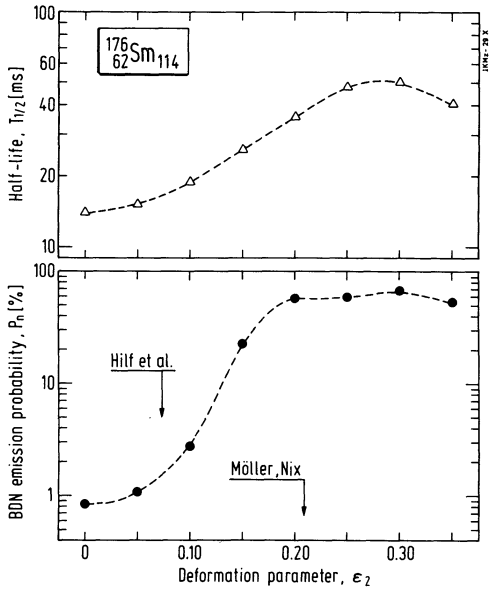

FIG. 23.—Same as Fig. 22, but for nucleus ^{176}Sm. The difference in half-lives, when the deformation from Fig. 21 is used for both mass models, is even more drastic than for ^{112}Zr. The large overabundance found in the *r*-process calculations would be reduced by a factor of more than 2.

some shell strength must have remained below $^{132}_{50}Sn_{82}$. As already mentioned, the fact that the calculated pronounced trough below the $A \simeq 130$ *r*-abundance peak is not seen in reality may support our interpretation that it is "hidden" by the compensating effect of "longer" $T_{1/2}$ due to shape coexistence in this region. In summary, we have seen that from both the overall success and the local failures in the reproduction of the solar *r*-abundance distribution, we can conclude that the underlying nuclear structure far from beta stability is reasonably well understood by now—thanks to the detailed experimental knowledge near stability and thanks to our continuously improving unified nuclear-model predictions for unknown regions. The local deficiencies discussed above for our three-component (or four-component) best-fit n_n-T_9 conditions may well be shifted or smeared out to some extent, e.g., by assuming additional (intermediate) *r*-process components or by choosing slightly different process durations, but they will persist as "real" nuclear structure signatures of very neutron-rich isotopes, not accessible in terrestrial but only in stellar laboratories. Hence, we can, indeed, learn nuclear structure from isotopic *r*-process abundances. This offers fascinating perspectives for experimentalists and theoreticians in the entwined fields of nuclear physics and astrophysics.

7. DISCUSSION

While all of the previous discussion was focused on an analysis of solar *r*-process abundances with a minimum set of n_n-T_9 conditions, there is no reason why in nature this could not be a more continuous distribution. In such a case, one would actually expect a further improvement and smoothing of the total abundance curve. The quality of the curve for the "pygmy" peaks around $A \simeq 103$ and $A \simeq 163$ may be enhanced by a component with slightly smaller neutron densities; hence, the assumption of large fission contributions is not necessary. However, the major large deficiencies discussed above will still remain and need a solution via an improved understanding of nuclear properties. This can also be noticed in Meyer et al. (1992), who made use of a superposition of 10 components.

A second unrealistic point in our treatment is that we only performed calculations for constant temperatures and neutron densities. In reality these quantities will vary. For n_n and T_9 beyond the $(n, \gamma) \rightleftharpoons (\gamma, n)$ freeze-out line in Figure 4, a change of conditions leads to an immediate adjustment, so that we expect the freeze-out conditions to give the final fingerprint which is actually observed in solar *r*-abundances. Nevertheless, the time history of a mass zone in this diagram determines the history of *r*-process paths and, with this, the beta-decay time scales encountered. Thus, the time scales for the conditions at freeze-out are not necessarily representative for the real time scales a blob of matter encountered. If we think of the superposition required to reproduce solar *r*-abundances in only one astrophysical event, one should also expect the same time scales for different components. This is apparently in slight contradiction to our findings of moderately increasing times required for the different components as a function of mass number A (see § 5.3), but they vary by less than a factor of 2. On the other hand, as discussed above, temperature and density variations in time could lead to a stretching or shrinking of time scales. Thus, a superposition of time-dependent calculations performed at freeze-out conditions is allowed to use components with moderately (but not greatly) different duration times, without contradicting simultaneity.

Finally, we have to address an issue which, so far, has been carefully avoided. We made use of an ideal instantaneous freeze-out, where equilibrium conditions apply at one instant and neutron densities and temperatures drop strongly, so that abundances do not change any more but are instantaneously frozen instead. However, for a slow decrease of both T_9 and n_n, a very different behavior would apply, allowing for considerable distortion of the initial abundance pattern via neutron captures. Trying to be completely deductive about the *required* conditions for a realistic scenario, we have some indications that the latter is not the case. The strongest "proof" is the observed abundance pattern in the $A \simeq 80$ peak (see Figs. 7*a* and 7*b*), which shows significant odd-even features, almost exactly the way imprinted by a steady flow and subsequent beta decay and beta-delayed neutron emission. It is just in this region where most of the nuclear properties come from experiment, i.e., are strongly reliable. We expect $\langle \sigma v \rangle_{n,\gamma}$ values of up to 2.4×10^{-19} cm^3 s^{-1} for this region from the appendix of Cowan et al. (1991; for ^{85}As, the decay product of ^{86}Ge via beta-delayed neutron emission). This corresponds to a neutron-capture time scale of $\tau_{n,\gamma} = 1/(n_n \langle \sigma v \rangle) = 0.042$ s, taking a typical $n_n = 10^{20}$ cm^{-3} before freeze-out in that region. Thus, the drop in neutron number density at freeze-out must be short in comparison with 0.04 s.

Another question is whether on such time scales the significant deviations in the predicted abundances could be wiped out by neutron captures during the freeze-out. The "spike" at $A \simeq 111$ results from beta decay and delayed neutron emission of the "overabundant" waiting-point nucleus ^{112}Zr (see, e.g., Fig. 17) with $\langle \sigma v \rangle = 2.43 \times 10^{-20}$ cm^3 s^{-1}, which, together with a typical $n_n = 10^{21}$ cm^{-3} for that region, results in $\tau_{n,\gamma} = 0.042$ s as well. Thus, when the correct features at $A \simeq 80$ are preserved, this deviation would also remain on the same time scale. In order to fill the trough in the range $115 \leq A \leq 125$, matter would have to pass through ^{115}Nb, ^{116}Mo, and ^{120}Mo

with $\langle \sigma v \rangle$ values of (2.8–7.2) $\times 10^{-20}$ cm^3 s^{-1}, which corresponds to $\tau_{n\gamma}$ values of 0.014–0.036 s. Thus, again on a time scale short in comparison with 0.04 s, it would not be possible to fill this trough of 10 mass units (A = 115–125) via neutron capture. The $A \simeq 175$ abundance "spike" results from beta decay and delayed neutron emission of ^{176}Sm, which has a $\langle \sigma v \rangle$ value of 1.04×10^{-19} cm^3 s^{-1}. With $n_n = 2 \times 10^{21}$ cm^{-3} at freeze-out (see in Fig. 12 the intersection of the $A = 195$ line with the freeze-out line), this corresponds to $\tau_{n,\gamma} = 0.005$ s, about a factor of 10 smaller than our above requirement would allow. This means that neutron capture during freeze-out will occur, but when reaching ^{178}Sm the time scale goes up to 0.014 s, already comparable to the allowed 0.04 s. Thus, this spike will experience neutron captures during the freeze-out; however, it will not be wiped out completely but only moved upward in A by a few units; see also Meyer et al. (1992). In general, neutron captures during freeze-out will certainly smooth the abundance curve somewhat. We could, however, show here that the major deficiencies discussed above would remain. Therefore, this is a belated proof that they must be due to remaining deficiencies in nuclear properties, which supports our conclusions of § 6. A more general analysis has to be performed to test possible neutron capture during freeze-out for the whole abundance pattern. Such calculations are planned in collaboration with J. J. Cowan.

8. CONCLUSIONS

Until now, we did not make any contact with astrophysical sites where the r-process supposedly takes place. This also was our intention, because the main logic behind this paper was to deduce the conditions in an r-process site by requiring that the solar abundance features be reproduced. The high neutron number densities and temperatures obtained as a result of the present study can only occur in the cores of Type II supernovae or neutron star–neutron star or neutron star–black hole collisions. It was discussed in great detail in Cowan et al. (1991a, b) that the observed metallicity dependence of r-process abundances in old stars requires the Type II supernova source (while it does not exclude the other options as additional sources).

The main problem in Type II supernovae is still the explosion mechanism itself (see, e.g., Bethe 1990; Mayle & Wilson 1990; Bruenn & Haxton 1991), although progress has been made in multidimensional calculations (Herant, Benz, & Colgate 1992). For nucleosynthesis purposes, this relates to an uncertainty in the position of the mass cut between neutron star and ejecta, and the neutronization of material in the collapse prior to explosion and ejection. These inner zones are best suited for an r-process to occur, but it is not yet well known whether in Type II supernovae of all masses this material is outside the position of the mass cut and will be ejected. Given these uncertainties in astrophysical sites, it is still important to analyze the solar r-process abundances and deduce information which can give clues to the exact conditions (neutron density n_n, temperature T, and process duration t) necessary to produce the observed abundance distribution. It is exactly here where a strong interplay between nuclear structure properties of neutron-rich nuclei far from stability and astrophysics exists.

In an extended discussion on r-process conditions, we have shown that the observed solar r-process abundances can be reproduced under the assumption of the waiting-point approximation, which postulates an equilibrium between (n, γ) and (γ, n) reactions in each isotopic chain. This automatically excludes production sites with low n_n and T, thus supporting the Type II supernovae origin of the r-process (or other high n_n-T events). It is, however, not possible to get the whole abundance curve for only one set of conditions. When applying a global steady-flow approximation, we can obtain three abundance peaks, but they do not have the correct height, nor do they occur at the right mass number. A steady flow is valid only in certain regions. It breaks down slightly beyond the maximum of each peak. where the half-lives of the progenitor isotopes are "long" and become comparable to the expected duration of the r-process in a supernova event.

Between the abundance peaks and from the onset through the center of each peak, the steady-flow approximation is still valid. The n_n values required to fit these regions increase with the mass of the nuclei produced. The n_n distribution we found in the steady-flow approximation can also be applied in time-dependent calculations where each neutron number density produces only the appropriate mass region. All three main abundance peaks can be produced in comparable but slightly increasing time scales. The observed abundances require a superposition of ejecta with neutron number densities varying over several orders of magnitude beyond 10^{20} cm^{-3}. The higher n_n values lead to r-process paths more remote from stability where the flow moves faster toward heavier nuclei. We also showed that the elements below mass $A = 77$ cannot be produced by a traditional r-process.

Recent investigations in the Type II supernova r-process focused on the high-entropy (temperature)–low-density bubble outside the neutrino sphere, created by neutrino heating. There the peak densities before adiabatic expansion are less than 10^7 g cm^{-3}, which leads to an alpha-rich freeze-out of charged-particle reactions. Woosley & Hoffman (1992) showed that, depending on the neutron excess of the alpha-rich freeze-out, this process automatically results in a variation of seed nuclei and may also explain the abundances for $A \leq 77$ which could not be obtained here. In addition, the seed nuclei for the subsequent r-process would generally not only be part of the Fe group ($Z \simeq 26$) but would go as far as $Z = 40$ for the higher neutron densities. In such a case, our apparently increasing process times for the different r-process components, discussed in § 5.3, would become equal and make the production of all r-process components simultaneous events. This favors the scenario of an r-process in the high-entropy bubble (Meyer et al. 1992) if the conditions resulting from the present analysis can be fulfilled, although other sites have still to be tested.

It remains to be said that with the present advances in the understanding of nuclear properties far from stability even detailed *isotopic* fits are becoming possible and meaningful—at least in the vicinity of the r-process peaks (see Figs. 7, 9, and 10). Nevertheless, additional experimental data far off stability and further theoretical improvements are needed to obtain agreement as good in between peaks as for the abundance peaks themselves. There, where the r-process path is located very far from stability, uncertainties in the extrapolation of nuclear properties are still the largest. Even the improved mass model of Möller et al. (1992b) still predicts wrong ground-state spins for about 40% of the known nuclei, and accompanying uncertainties in the QRPA calculations of beta-decay properties ($T_{1/2}$, P_n) are inevitable. It will be interesting to see whether forthcoming results from the extended Thomas-Fermi (ETF) approach (Pearson et al. 1992) or the fermion dynamic symmetry model (FDSM) (Wu et al. 1987; Han et al. 1992; Wang et al. 1992) may lead to further improvements.

We thank H. Beer, A. G. W. Cameron, J. Cowan, F. Käppeler, R. Leclerc, G. Mathews, B. Meyer, R. Mochkovitch, and S. Woosley for stimulating discussions, and A. Wöhr for his help in establishing the nuclear data base for the present calculations. This research was supported in part by the NSF grant AST 89-13799, DFG grant Kr 806/1, BMFT grant 06MZ106, and the Fondation de l'Ecole Polytechnique. The computations were performed at the National Center for Supercomputer Applications at the University of Illinois (AST 890009N) and at the Kernchemie Mainz VAX Cluster.

REFERENCES

Beer, H. 1991, ApJ, 379, 409
Beer, H., & Macklin, R. L. 1985, Phys. Rev. C, 32, 738
Bethe, H. A. 1990, Rev. Mod. Phys., 62, 801
Blake, J. B., Woosley, S. E., Weaver, T. A., & Schramm, D. N. 1981, ApJ, 248, 315
Blomqvist, J. 1981, in Proc. Fourth Int. Conf. on Nuclei Far from Stability (Helsingör) (CERN 81-09), 536
Bolsterli, M., Fiset, E. O., Nix, J. R., & Norton, J. L. 1972, Phys. Rev. C, 5, 1050
Bruenn, S. W., & Haxton, W. C. 1991, ApJ, 376, 678
Burbidge, E. M., Burbidge, G. R., Fowler, A. A., & Hoyle, F. 1957, Rev. Mod. Phys., 29, 547
Cameron, A. G. W. 1957, Atomic Energy of Canada, Ltd., CRL-41
Cameron, A. G. W., Delano, M. D., & Truran, J. W. 1970, in Proc. First Int. Conf. on Nuclei Far from Stability (CERN Rep. 70-30), 2, 735
Cameron, A. G. W., Cowan, J. J., Klapdor, H. V., Metzinger, J., Oda, T., Truran, J. W. 1983a, Ap&SS, 91, 221
Cameron, A. G. W., Cowan, J. J., & Truran, J. W. 1983b, Ap&SS, 91, 235
Cameron, A. G. W., Thielemann, F.-K., & Cowan, J. J. 1992, Phys. Rep., in press
Casten, R. F. 1985a, Phys. Lett. B, 152, 145
———. 1985b, Phys. Rev. Lett., 54, 199
Cowan, J. J., Cameron, A. G. W., & Truran, J. W. 1985, ApJ, 294, 656
Cowan, J. J., Thielemann, F.-K., & Truran, J. W. 1991a, Phys. Rep., 208, 267
———. 1991b, ARA&A, 29, 447
Daley, H. J., Nagarajan, M. A., Rowley, N., Morrison, D., & May, A. D. 1986, Phys. Rev. Lett., 57, 198
Duke, C. L., Hansen, P. G., Nielsen, O. B., & Rudstam, G. 1970, Nucl. Phys. A, 151, 609
Eberth, J., Meyer, R. A., & Sistemich, K. 1988, in Proc. Int. Workshop on Nuclear Structure of the Zirconium Region (Bad Honnef, Germany) (Res. Rep. in Physics)
Ekström, B., Fogelberg, B., Hoff, P., Lund, E., & Sangariyavanish, A. 1986, Phys. Scripta, 34, 614
Gallino, R., Busso, M., Picchio, G., & Raiteri, C. M. 1990, Nature, 348, 298
Gill, R. L., et al. 1986, Phys. Rev. Lett., 56, 1974
Goriely, S., & Arnould, A. 1992, A&A, submitted
Halbleib, J. A., & Sorenson, R. A. 1967, Nucl. Phys. A, 98, 542
Hamamoto, I. 1965, Nucl. Phys., 62, 49
Han, X.-L., Wu, C.-L., Feng, D. H., & Guidry, M. W. 1992, Phys. Rev. C, in press
Harper, C. L., Nyquist, L. H., Shih, C.-Y., & Wiesmann, H. 1990, in Nuclei in the Cosmos, ed. H. Oberhummer & W. Hillebrandt (MPA/P4; Garching: MPI für Physik und Astrophysik), 138
Hartmann, D., Woosley, S. E., & El Eid, M. F. 1985, ApJ, 297, 837
Herant, M., Benz, W., & Colgate, S. 1992, ApJ, 395, 642
Heyde, K., Sau, J., & Van Meldeghem, J. 1981, in Proc. Fourth Int. Conf. on Nuclei Far from Stability (Helsingör) (CERN Rep. 81-09), 519
Hilf, E. R., von Groote, H., & Takahashi, K. 1976, in Proc. Third Int. Conf. on Nuclei Far from Stability (CERN Rep. 76-13), 142
Hillebrandt, W. 1978, Space Sci. Rev., 21, 639
Hillebrandt, W., Takahashi, K., & Kodama, T. 1976, A&A, 52, 63
Hollowell, D. E., & Iben, I. 1989, ApJ, 340, 996
Käppeler, F., Beer, H., & Wisshak, K. 1989, Rep. Prog. Phys., 52, 945
Käppeler, F., Jaag, S., Bao, Z. Y., & Reffo, G. 1991, ApJ, 366, 605
Klapdor, H. V., Metzinger, J., & Oda, T. 1984, Atomic Data Nucl. Data Tables, 31, 81
Kodama, T., & Takahashi, K. 1975, Nucl. Phys. A, 239, 489
Kratz, K.-L. 1984, Nucl. Phys. A, 417, 447
———. 1988, Rev. Mod. Astron., 1, 184
Kratz, K.-L., Gabelmann, H., Hillebrandt, W., Pfeiffer, B., Schlösser, K., & Thielemann, F.-K. 1986, Z. Phys. A, 325, 483
Kratz, K.-L., Gabelmann, H., Möller, P., Pfeiffer, B., Ravn, H. L., Wöhr, A., & the ISOLDE Collaboration. 1991a, Z. Phys. A, 340, 419
Kratz, K.-L., Gabelmann, H., Möller, P., Pfeiffer, B., Ravn, H. L., Wöhr, A., & Thielemann, F.-K. 1991b, in Proc. NATO Advanced Research Workshop on Nuclear Shapes and Nuclear Structure at Low Excitation Energies (New York: Plenum), 339
Kratz, K.-L., Harms, V., Hillebrandt, W., Pfeiffer, B., Thielemann, F.-K., & Wöhr, A. 1990, Z. Phys. A, 336, 357
Kratz, K.-L., et al. 1988a, Phys. Rev. C, 38, 278
Kratz, K.-L., Pfeiffer, B., Wöhr, A., & Möller, P. 1989, Z. Phys. A, 332, 419
Kratz, K.-L., & Thielemann, F.-K. 1988, J. Phys. G, 14, 742
Kratz, K.-L., Thielemann, F.-K., Hillebrandt, W., Möller, P., Harms, V., Wöhr, A., & Truran, J. W. 1988b, J. Phys. G, 14, 331
Kratz, K.-L., Zieger, W., Hillebrandt, W., Thielemann, F.-K. 1983, A&A, 125, 381
Krumlinde, J., & Möller, P. 1984, Nucl. Phys. A, 417, 419
Lhersonneau, H., Gabelmann, H., Kaffrell, N., Kratz, K.-L., Pfeiffer, B., Heyde, K., & the ISOLDE Collaboration. 1990, Z. Phys. A, 337, 149
Lhersonneau, G., Gobelmann, H., Pfeiffer, B., Kratz, K.-L., & the OSTIS and ISOLDE Collaborations. 1991, in Proc. First European Biennial Workshop on Nuclear Physics (Megeve, France) (Singapore: World Scientific), 214
Mathews, G. J., & Cowan, J. J. 1990, Nature, 345, 491
Mathews, G. J., Mengoni, A., Thielemann, F.-K., & Fowler, W. A. 1983, ApJ, 270, 740
Mayle, R. W., & Wilson, J. R. 1990, in Supernovae, ed. S. E. Woosley (New York: Springer-Verlag), 333
Meyer, B. S., Howard, W. M., Mathews, G. J., Takahashi, K., Möller, P., & Leander, G. A. 1989, Phys. Rev. C, 39, 1876
Meyer, B. S., Mathews, G. J., Howard, W. M., Woosley, S. E., & Hoffman, R. D. 1992, ApJ, Nov. 10
Möller, P., & Nix, J. R. 1974, Nucl. Phys. A, 229, 269
———. 1981, Atomic Data Nucl. Data Tables, 26, 165
———. 1992, Nucl. Phys. A, 536, 20
Möller, P., Nix, J. R., & Kratz, K.-L. 1992a, in Proc. Int. Conf. on Exotic Nuclei (South Crimea), in press
Möller, P., Nix, J. R., Kratz, K.-L., & Howard, W. M. 1990, in Nuclei in the Cosmos, ed. H. Oberhummer & W. Hillebrandt (MPA/P4; Garching: MPI für Physik und Astrophysik), 226
Möller, P., Nix, J. R., Myers, W. D., & Swiatecki, N. 1992b, Atomic Data Nucl. Data Tables, in press
Möller, P., & Randrup, J. 1990, Nucl. Phys. A, 514, 1
Myers, W. D. 1976, Atomic Data Nucl. Data Tables, 17, 411
Neugart, R., et al. 1988, in Nuclear Structure of the Zirconium Region, ed. J. Eberth, R. A. Meyer, & K. Sistemich (Berlin: Springer-Verlag), 188
Nix, J. R. 1972, Ann. Rev. Nucl. Sci., 22, 65
Ohm, H., Lhersonneau, G., Sistemich, K., Pfeiffer, B., & Kratz, K.-L. 1987, Z. Phys. A, 327, 483
Pearson, J. M., Aboussir, Y., Duttei, A. K., Naya, R. C., Ferris, M., & Tondeur, F. 1992, Nucl. Phys. A, in press
Pfeiffer, B., & Kratz, K.-L. 1987, Z. Phys. A, 327, 163
Pfeiffer, B., Möller, P., & Kratz, K.-L. 1991, Table of QRPA Predictions of $T_{1/2}$ and P_n, unpublished
Seeger, P. A., Fowler, W. A., & Clayton, D. D. 1965, ApJS, 97, 121
Staudt, A., Bender, E., Muto, K., & Klapdor, H. V. 1989, Z. Phys. A, 334, 47
———. 1990, Atomic Data Nucl. Data Tables, 44, 79
Strutinsky, V. M. 1967, Nucl. Phys. A, 95, 420
———. 1968, Nucl. Phys. A, 122, 1
Takahashi, K., Yamada, M., & Kondo, Z. 1973, Atomic Data Nucl. Data Tables, 12, 101
Thielemann, F.-K., Bitouzet, J.-P., Kratz, K.-L., Möller, P., Cowan, J. J., & Truran, J. W. 1992, Phys. Rep., in press
Thielemann, F.-K., Arnould, M., & Hillebrandt, W. 1979, A&A, 74, 175
Thielemann, F.-K., Arnould, M., & Truran, J. W. 1987, in Advances in Nuclear Astrophysics, ed. E. Vangioni-Flam et al. (Gif-sur-Yvette: Editions Frontières), 525
Thielemann, F.-K., Hashimoto, M., & Nomoto, K. 1990, ApJ, 349, 222
Towner, S. 1988, In Proc. Fifth Conf. on Nuclei Far from Stability (Rosseau Lake) (AIP Conf. Proc. 164; New York: AIP)
Truran, J. W., Cameron, A. G. W., & Hilf, E. 1970, in Proc. First Int. Conf. on Nuclei Far from Stability (CERN Rep. 70-30)
Truran, J. W., Cowan, J. J., & Cameron, A. G. W. 1978, ApJ, 222, L63
von Groote, H., Hilf, E. R., & Takahashi, K. 1976, Atomic Data Nucl. Data Tables, 17, 418
Wang, R.-P., Thielemann, F.-K., Feng, D. H., & Wu, C.-L. 1992, Phys. Lett., in press
Winger, J. A., et al. 1987, Phys. Rev. C, 37, 758
Wöhr, A., Lhersonneau, G., Pfeiffer, B., Gabelmann, H., & Kratz, K.-L. 1991, Verhandl. DPG (VI) 26, D2.4
———. 1992, in preparation
Woosley, S. E., & Hoffman, R. 1992, ApJ, 395, 202
Wu, C.-L., Han, X.-L., Li, Z.-P., Guidry, M. W., & Feng, D. H. 1987, Phys. Lett. B, 194, 447